COMPUTER SIMULATIONS AND FLUORESCENCE CONFOCAL POLARIZING MICROSCOPY OF STRUCTURES IN CHOLESTERIC LIQUID CRYSTALS

S.V. SHIYANOVSKII, I.I. SMALYUKH AND O.D. LAVRENTOVICH

Liquid Crystal Institute and Chemical Physics Interdisciplinary Program, Kent State University, Kent, OH 44242, U.S.A.

Abstract. We describe two complementary techniques: (1) computer simulations and (2) fluorescence confocal polarizing microscopy (FCPM) to visualize three-dimensional patterns of the director field in liquid crystals (LCs). Computer simulations account for finite surface anchoring strength, non-local electric field effects, non-equal bulk elastic constants and saddle-splay elasticity and predict a variety of structures with complex director configurations. We demonstrate that in contrast to traditional methods such as polarizing microscopy, a new FCPM technique allows one to image the director configuration both in horizontal and vertical cross-sections of the sample and results in a three-dimensional image of the director configuration.

1. Introduction

In the preface to the book on "The Physics of Liquid Crystals" [1], P.G. de Gennes has written that "...the study of liquid crystals is complicated because it involves several different scientific disciplines... and also a certain sense of vision in three-dimensional space in order to visualize complex molecular arrangements." The simplest tool to substantiate such a sense of three-dimensional arrangements is polarizing microscopy (PM). PM tests the orientation of optical axes of the liquid crystal specimen; these optical axes are closely related to the molecular arrangements in the medium. Unfortunately, PM yields only two-dimensional (2D) textures in the so-called plane of observation which is perpendicular to the optical axis of the microscope [2, 3, 4]. This 2D image integrates the true 3D configuration of optical birefringence over the path of light [4]. As the result of such an

229

integration, the director profile along the direction of observation (="vertical cross section" of the specimen) is hard to decipher. Regrettably, it is precisely the director configuration in the vertical cross-section that is often the most valuable and desirable. Other available nondestructive techniques, such as nuclear magnetic resonance, x-ray diffraction, measurements of optical phase retardation, etc., suffer from the same deficiency: they produce only an integrated image of the 3D director structure.

We describe a new technique, called the fluorescence confocal polarizing microscopy (FCPM) that allows one to recover the missing information and to obtain a truly 3D image of the liquid crystal director, both in the plane of observation and along the direction of observation [5]. The principle of imaging is different from the traditional PM. The FCPM maps the intensity of polarized fluorescent light emitted by the liquid crystal sample, rather than the pattern of integrated birefringence as the PM texture does. This feature allows one to avoid the ambiguity of the in-plane PM textures that do not distinguish between two mutually perpendicular director configurations. More importantly, the confocal scheme allows one to collect the fluorescent light from a very small region of the sample and thus to optically slice the specimen by scanning the focused laser beam. The obtained map of fluorescence intensity is the 3D image of orientation of the fluorescent probe.

To illustrate the FCPM technique, we use the cholesteric LC confined between two glass plates and subject to the electric field. Director configurations of cholesteric LCs with twisted helicoidal director field as the ground state, are very complex. Balance of several factors, namely, chirality, elasticity, surface anchoring and coupling to the applied field, results in a rich variety of structures, see, e.g., [6]. Optical anisotropy (birefringence) of LCs makes the light propagation through these configurations difficult to analyze. On the other hand, the twisted structure makes the cholesteric LCs attractive for applications in display, beam steering and beam shaping devices.

Traditionally, lack of an experimental tool to recover the 3D image of a LC cell has been partially compensated by theoretical models that calculate equilibrium director configurations on the basis of the Frank-Oseen free energy density. The theoretical director profile can be used to decipher the experimental 3D structure, for example, by measuring the optical phase retardation and then comparing it to the model. The same approach can be used to verify the FCPM textures. The problem is that the complexity of many LC structures does not allow one to find the director configuration analytically. In the recent years, numerical modelling has become a widespread method to find the equilibrium director structures and transitions between them. In this work we present our numerical procedure de-

signed to simulate 2D and 3D director patterns in LC cells. The computer program accounts for anisotropic elasticity, various boundary conditions, divergence elastic term K_{24}, dielectric and diamagnetic effects.

The paper is organized as follows. We start with the mathematical basis of computer simulations, Section 2. When the simulated director field is periodic, as in the cholesteric phase, a special scaling procedure finds a self-consistent period to make sure that the periodicity is not affected by the finite size of the computational domain. The principles of FCPM in anisotropic media are outlined in Section 3. Section 4 describes experimental details of sample preparation and observations by the FCPM. Experimental and simulated results are presented and discussed in section 5 for different director configurations, starting with the simplest untwisted nematic cells and finishing with the complex cholesteric structures in the electric field.

2. Mathematical basis for computer simulations of equilibrium LC structures

The equilibrium LC structure is found by minimizing the free energy functional F, which is a sum of the elastic f_{el} and electrostatic f_E bulk energy densities and the surface anchoring energy f_S:

$$F = \int \left(f_{el} + f_E\right) dv + \int f_S \, dS. \tag{1}$$

2.1. LC STRUCTURE AND ELASTIC PROPERTIES

Studies of the macroscopic structure and elastic properties of liquid crystals are based on vector and tensor approaches. The vector approach considers the LC structure as a field of the unit vector $\mathbf{n} \equiv -\mathbf{n}$, called the "director", and employs the well-known Frank-Oseen expression for the elastic free energy density that is an invariant quadratic form of the first spatial derivatives of $\mathbf{n}$:

$$f_{el} = f_{FO} = \frac{K_{11}}{2} \left(\text{div}\mathbf{n}\right)^2 + \frac{K_{22}}{2} \left(\mathbf{n}\cdot\text{curl}\mathbf{n}\right)^2 + K_c \left(\mathbf{n}\cdot\text{curl}\mathbf{n}\right)$$

$$+ \frac{K_{33}}{2} \left[\mathbf{n}\times\text{curl}\mathbf{n}\right]^2 - K_{24} \,\text{div} \left(\mathbf{n}\cdot\text{div}\mathbf{n} + \mathbf{n}\times\text{curl}\mathbf{n}\right), \tag{2}$$

where K_{11}, K_{22}, and K_{33} are the Frank elastic constants for splay, twist, and bend deformations, respectively, K_c is the chiral coefficient that determines the pitch of cholesteric LC: $p = 2\pi K_{22}/K_c$. The divergence (saddle-splay) elastic K_{24} term can be reduced to the surface integral and has to be taken

into account in the case of finite anchoring, and when the topological defects are present.

The tensor approach describes the LC structure by a symmetric traceless tensor order parameter Q_{ij}. The elastic energy density is derived as Landau-de Gennes expansion of the free energy with respect to Q_{ij} and its spatial derivatives $Q_{ij,k} = \frac{\partial Q_{ij}}{\partial x_k}$ [7, 8]:

$$f_{el} = f_{LdG} = L_c \epsilon_{mjk} Q_{im} Q_{ij,k} + \frac{1}{2} \left(L_1 Q_{ij,k} Q_{ij,k} + L_2 Q_{ij,j} Q_{ik,k} + L_3 Q_{ij,k} Q_{ik,j} \right), \tag{3}$$

where ϵ_{mjk} is the antisymmetric Levi-Civita tensor. The first term in (3) vanishes in an achiral nematic phase due to inversion symmetry.

In computer simulations, the two approaches have their advantages and drawbacks. The director description, applicable for the uniaxial phase $Q_{\alpha\beta} = S(n_\alpha n_\beta - \frac{1}{3}\delta_{\alpha\beta})$, is based on the assumption that the orientational order parameter S is constant and that the LC is far from the transition to the isotropic phase. In real LCs, the director states $\mathbf{n}$ and $-\mathbf{n}$ are physically identical. Because of this, the real LCs can contain topological defects, around which $\mathbf{n}$ transforms into $-\mathbf{n}$ (the so-called defects of half-integer strength). Unfortunately, discretization of Eq.(2) in computer simulations effectively eliminates the equivalency of $\mathbf{n}$ and $-\mathbf{n}$ and thus does not allow one to simulate the half-integer defects. The manifolds at which $\mathbf{n}$ meets $-\mathbf{n}$ are treated as singular regions with enormous energy. To overcome the problem, Hess and co-workers have introduced an alignment tensor $a_{\alpha\beta} = n_\alpha n_\beta - \frac{1}{3}\delta_{\alpha\beta}$ and simulated half-integer line defects in one-constant approximation (equal Frank elastic constants) [9].

The tensor approach operates with the true order parameter and causes no problems with the defect structures. However, the Landau-de Gennes expansion is designed to describe the behavior of the system near the phase transition only; the assumption is that the scalar order parameter is small. The expansion (3) contains four elastic constants instead of five in Eq.(2) and implies that $K_{11} = K_{33}$, which is generally not true. To obtain $K_{11} \neq K_{33}$ one should take into account higher order terms with respect to Q_{ij} in Eq.(3) [7, 8, 10, 11, 12], but then the number of elastic constants increases drastically.

In this work, we use the vector model in computer simulations. The half-integer singular defect lines do not appear in this approach. Such an omission is partly justified by the fact that in the experiments, many deformed structures in a confined cholesteric cell are seen to adapt to the boundary conditions and the external fields without director singularities which are energetically costly.

2.2. ELECTRIC FIELD

The dielectric anisotropy of many LCs is large. As a result, the electric field in a cell with a distorted director is significantly inhomogeneous even if the electrodes are homogeneous. In this work we find the electric potential $V(\mathbf{r})$ inside the cell self-consistently. The Frank-Oseen functional is supplemented by the dielectric term

$$F_E = \int -\frac{\varepsilon_0}{2} \left(\nabla V \cdot \varepsilon \cdot \nabla V \right) dv, \tag{4}$$

where ε_0 is the absolute dielectric constant, ε is the relative dielectric tensor with components $\varepsilon_{ij} = \varepsilon_\perp \delta_{ij} + \varepsilon_a n_i n_j$, $\varepsilon_a = \varepsilon_\parallel - \varepsilon_\perp$, $\varepsilon_\parallel$ and $\varepsilon_\perp$ are the dielectric permittivities parallel and perpendicular to the director, respectively.

Variation of F_{FO} with respect to the potential V inside the cell produces the Maxwell equation:

$$\frac{\delta F_{FO}}{\delta V} = \operatorname{div}(\varepsilon_0 \varepsilon \nabla \mathrm{V}) = 0. \tag{5}$$

2.3. SURFACE ANCHORING

Description of the LC anchoring operates with the axis of easy director orientation $\mathbf{e}$ and the anchoring energy W that characterizes the work required to deviate the director $\mathbf{n}$ at the surface from the easy axis. The angular coordinates of the easy axis $\mathbf{e}$ are $(\frac{\pi}{2} - \beta, \psi)$, where β is the so-called pretilt angle between $\mathbf{e}$ and the projection of $\mathbf{e}$ onto the substrate; ψ is the azimuthal orientation of this projection. In a similar fashion, two angular coordinates $(\theta = \frac{\pi}{2} - \alpha, \varphi)$ specify the actual orientation of the director. Deviations from the easy axis that keep $\varphi = \psi$ are described in terms of the polar anchoring coefficient W_p. Deviations that change φ are described with the azimuthal coefficient W_a. The definitions of the anchoring coefficients are usually based on the Rapini-Papoular model [13]. For zero pretilt angle $\beta = 0$, the surface energy per unit area is:

$$f_s = \frac{1}{2} W_{\mathrm{p}} \sin^2 \alpha + \frac{1}{2} W_{\mathrm{a}} \cos^2 \alpha \sin^2 \left(\varphi - \psi \right). \tag{6}$$

When β is not zero, we have to distinguish two cases. First, when a nonzero pretilt appears as a result of the anchoring transition, the easy axis splits into two ($\pm \beta$) axes and f_s remains an even function of α:

$$\begin{aligned} f_s = \; & \frac{W_{\mathrm{p}}}{2} \left[\sin^2 \left(\alpha - \beta \right) + \sin^2 \left(\alpha + \beta \right) \right] \\ & + \frac{W_{\mathrm{a}}}{2} \sin^2 \left(\varphi - \psi \right) \left[\cos^2 \left(\alpha - \beta \right) + \cos^2 \left(\alpha + \beta \right) \right]. \end{aligned} \tag{7}$$

Second, if the substrate treatment (such as oblique deposition of SiO_x or unidirectional buffing of a polymer alignment layer), prevents the degeneracy β and $-\beta$, then

$$f_s = \frac{W_p}{4}\left[1 - \cos 2\beta \cos 2\alpha - \cos(\varphi - \psi)\sin 2\beta \sin 2\alpha\right]$$
$$+ \frac{W_a}{2}\cos^2\beta \cos^2\alpha \sin^2(\varphi - \psi). \tag{8}$$

When $W_p = W_a = W$, Eq.(8) reduces to:

$$f_s = \frac{1}{2}W\left[1 - (\mathbf{n}\cdot\mathbf{e})^2\right], \tag{9}$$

which was used in [14] for determination of the anchoring strength. However, there is no reason for the polar and azimuthal anchoring coefficients to be equal. In this paper, we use Eq.(8) for surface anchoring; it is equivalent to a much more compact expression

$$f_s = -\frac{1}{2}W_{ij}\, n_i\, n_j, \tag{10}$$

where W_{ij} is the symmetrical anchoring tensor, that describes the easy axis as well as polar and azimuthal anchoring coefficients [15]. Minimum of the surface energy (10) can easily be found in the eigen frame $\{\mathbf{e_j}\}$ (j=1,2,3), where $W_{\alpha\beta}(\mathbf{r})$ is diagonal with eigenvalues $W_1 > W_2, W_3$. In the frame $\{\mathbf{e_j}\}$, which is orthogonal due to the symmetry $W_{\alpha\beta}(\mathbf{r}) = W_{\beta\alpha}(\mathbf{r})$, Eq.(10) reads:

$$f_s = -\frac{W_1}{2} + \frac{W_1 - W_2}{2}\, n_2^2 + \frac{W_1 - W_3}{2}\, n_3^2, \tag{11}$$

where n_j are the director components in this frame. The second and the third terms in (11) are non-negative, so that the axis $\mathbf{e_1}$, which corresponds to the maximum eigenvalue W_1, is exactly the easy axis, while the quantities $(W_1 - W_2)$ and $(W_1 - W_3)$ determine the traditional azimuthal and polar anchoring coefficients. Usually one of the eigenvectors, say $\mathbf{e_3}$, lays in the plane of the substrate. In this case $W_p = W_1 - W_2$ and $W_a = W_1 - W_3$.

The anchoring potential for the tensor representation $Q_{\alpha\beta}(\mathbf{r})$ can be written as an analogue of the Rapini-Papoular potential [16, 17]:

$$f_s = \frac{1}{2}A\,\mathrm{Tr}\left[\left(Q_{\alpha\beta}^b - Q_{\alpha\beta}^0\right)^2\right], \tag{12}$$

where A is the scalar anchoring strength, $Q_{\alpha\beta}^b$ is the surface value of the tensor order parameter, $Q_{\alpha\beta}^0 = \frac{3}{2}S_0(n_{0\alpha}n_{0\beta} - \frac{1}{3}\delta_{\alpha\beta})$ is the preferred surface value of the tensor order parameter.

2.4. DOMAIN AND SCHEME OF SIMULATIONS

The computer program is designed to study structures which in general case are periodic in the plane (x, y) of the cell, with the periodicities L_x and L_y along the x and y directions. In this particular work, we will be mostly interested in the structure with only one finite period L_x. The equilibrium values of L_x and L_y are not known *a priori*, and must be found from the minimization procedure. We simulate one main period of dimension $(0, L_x) \times (0, L_y) \times (0, d)$ with periodic boundary conditions:

$$\mathbf{n(r)} = \mathbf{n(r + L_x i)} = \mathbf{n(r + L_y j)}. \tag{13}$$

The discretized free energy $\bar{f} = \frac{F}{L_x L_y}$ per unit area (derivatives in each rectangular unit are substituted by corresponding differences between opposite faces of this unit) should have minimum with respect to $\mathbf{n}_{\{m\}}$, L_x and L_y and maximum with respect to the electric potential $V_{\{m\}}$. Relaxation to the equilibrium state is provided by the following 'motion' equations:

$$\gamma \frac{d\mathbf{n}_{\{m\}}}{dt} = -\frac{\delta \bar{f}}{\delta \mathbf{n}_{\{m\}}}, \tag{14}$$

$$\eta \frac{dV_{\{m\}}}{dt} = \frac{\delta \bar{f}}{\delta V_{\{m\}}}, \tag{15}$$

where the phenomenological viscosities γ and η are being adjusted during the calculation for the fastest convergence. The free energy f per unit area of the cell reads as the quadratic form

$$\bar{f} = f_0 + \sum_{\alpha=x,y} f_\alpha q_\alpha + \sum_{\alpha=x,y} f_{\alpha\beta} q_\alpha q_\beta, \tag{16}$$

where $q_{x,y} = 1/L_{x,y}$, f_0, f_α and $f_{\alpha\beta}$ are coefficients independent of q_α, so that the extremum of $\bar{f}$ with respect to q_x and q_y is easily calculated after each step. This convergent process allows us to find both the free energy extremum and the periodicity of equilibrium state (L_x and L_y) simultaneously.

3. Confocal Microscopy and Fluorescence Confocal Microscopy

Fluorescence confocal polarizing microscopy (FCPM) [5] is the version of the confocal microscopy (CM) in which the medium under examination is doped with a fluorescent probe and the observation is performed in polarized light. Below in sect 3.1 we give a brief account of the simple confocal microscopy technique, followed by the description of its modification, the

fluorescence technique, sect.3.2, and finally, present the new FCPM technique, sect.3.3 and 3.4.

3.1. CONFOCAL MICROSCOPY.

Confocal microscopy (CM) is the special technique of light microscopy in which the inspected region of specimen at a time is a small (submicron) voxel (=3D pixel) [18]. Signals from nearby voxels are suppressed by a special (confocal) optical design. An important element of this design is a pinhole in the image space (confocal aperture in Fig.1). The point source of light, the inspected voxel and the pinhole are confocal. Light coming from the neighborhood of the inspected voxel is blocked from reaching the detector [18]. To obtain the 3D image of the whole sample, the tightly focused laser beam scans the specimen voxel by voxel. Usually, it is implemented by optical scanning in the horizontal plane and then mechanical refocusing at different depth in the sample and repeating the horizontal scanning. As the result, the image is presented as a stack of thin (submicron) horizontal optical slices. Using a computer, the data that describe an essentially 3D pattern, can be presented as a horizontal or vertical "cross-sections" of the sample. The last feature makes the confocal microscope very different from the usual microscope in which the information over the path of light is integrated and the 3D image is essentially compressed to a 2D picture.

3.2. FLUORESCENCE CONFOCAL MICROSCOPY.

Fluorescence CM (FCM) is a version of CM in which the inspected specimen is doped with a high-quantum-yield fluorescent dye that strongly absorbs at the wavelength of the exciting laser beam. Excited dye molecules fluoresce at somewhat longer wavelength. The difference between the fluorescence and absorption wavelengths is called the Stokes shift. If the Stokes shift is sufficiently large, the exciting and fluorescence signals can be efficiently separated by filters so that only the fluorescence light would reach the detector. If the specimen is heterogeneous, the concentration of the fluorescent probe is coordinate-dependent, which results in a high-contrast image. The FCM technique makes it possible to visualize features in living cells and tissues; it is successfully applied in flow cytometry and even for single molecule detection [18].

The principle of FCM is illustrated in Fig.1. The illuminated voxel is a diffraction limited spot within the specimen produced by a focused laser beam. Fluorescence light passes through the pinhole aperture located in the focal plane that is conjugate to the illuminated point of specimen. The signal that reaches the detector from the regions above and below the voxel are of much weaker intensity since the corresponding beams diverge and
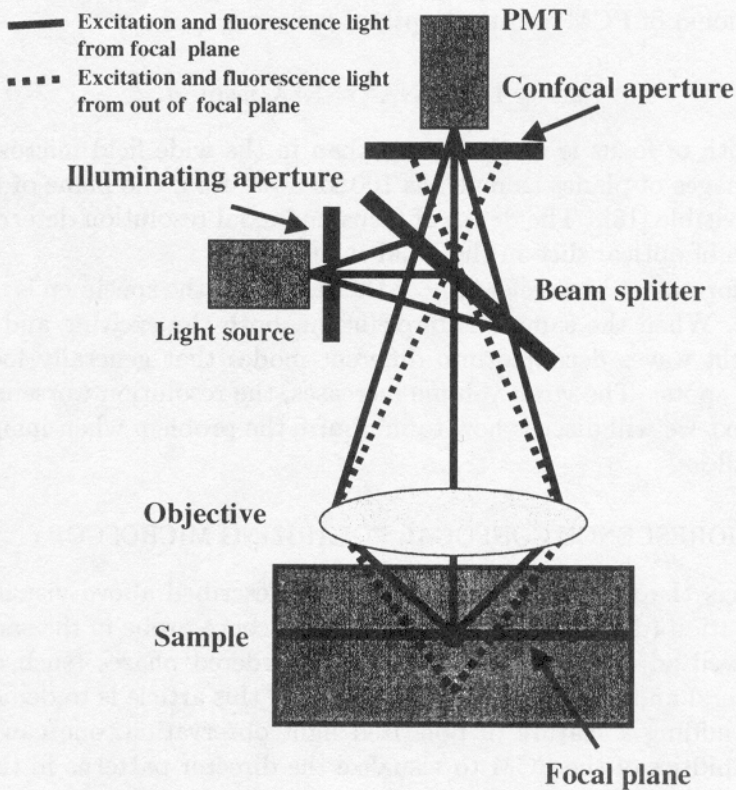
Figure 1. General optical scheme of a fluorescence confocal microscope.

cover an area much larger than the area of the pinhole. Two basic features, namely, (a) illumination of a single voxel at a time, and (b) blocking out-of-the-voxel fluorescence signal, improve the resolution of FCM as compared to an ordinary microscope. It is instructive to reproduce basic numerical estimates from Ref. [18].

The resolution in the plane of observation (radial resolution) is reduced by the factor of 0.72 as compared to the conventional wide field microscope:

$$\Delta r_{planeconf} = 0.72\Delta r_{wf} = 0.44\lambda/\text{NA} = 0.44\lambda/n\sin\vartheta, \qquad (17)$$

where NA is the numerical aperture of the objective, n is the refractive index of the medium in which the objective is immersed ($n = 1.52$ for some immersion oils and $n = 1.0$ for dry objective), ϑ is the half-angle of the cone of light converging to the illuminated spot which is determined by the entrance pupil of objective lens. The axial resolution (the ability of

the microscope to resolve two equally bright points along the direction of observations) of FCM and the depth of focus are

$$\Delta z = 1.5 n\lambda/\text{NA}^2 = 1.5\lambda/n\sin^2\vartheta. \tag{18}$$

This depth of focus is much thinner than in the wide field microscopy, in which images of planes as much as $100\Delta z$ away from the plane of focusing are still visible [18]. The depth of focus and axial resolution determine the thickness of optical slice in the FCM image.

The formulas above refer only to the case when the specimen is optically *isotropic*. When the sample is birefringent, both the exciting and fluorescence light waves decouple into different modes that generally focus into different spots. The voxel volume increases, the resolution worsens. Later in the text we will discuss how to minimize the problem when imaging the LC samples.

3.3. FLUORESCENCE CONFOCAL POLARIZING MICROSCOPY.

In essence, the traditional FCM technique described above visualizes the concentration (density) distribution of fluorescence probe in the sample. It is thus well adjusted to study positionaly ordered phases (such as block copolymers) and patterns. One of the goals of this article is to demonstrate that by adding a feature of polarized light observation, one can expand the capabilities of the FCM to visualize the director patterns in the liquid crystalline phases.

The approach, which we call Fluorescence Confocal Polarizing Microscopy (FCPM) [5], is very similar to FCM, with two new basic features: (a) the incident light is *polarized* and (b) the fluorescent dye molecules are *aligned* by the "host" material. The technique has been recently used to visualize 3D director distortions in the field–induced Fredericks transition in the nematic liquid crystals and complex distortions associated with the focal conic domains in smectic A cells [5]. Earlier applications of FCPM revealed 3D structures of some cholesteric samples: wall defects (oily streaks) [19] and periodic director modulations in cholesteric diffraction gratings, either uniform [20], or containing dislocations [21].

A simple view of how the FCPM visualizes a 3D director field in a nematic sample is as follows. Imagine a nematic liquid crystal cell doped with a fluorescent dye, Fig.2. For simplicity, assume that the nematic is of a calamitic type (elongated molecules) and that the fluorescent molecules are also elongated; one such dye molecule is shown as an ellipsoid in Fig.2. The transition dipoles of both excitation and fluorescence (double arrow at the ellipsoidal dye molecule) are along the long axis of the dye molecule. As it is well known, from the earlier studies of the so-called "guest-host"

display modes [22], the anisometric "guest" molecules are aligned by the nematic "host". The linearly polarized incident light causes fluorescence of the dye. The efficiency of light absorption is determined by the angle between the polarization **P** of incident light and the direction of the absorption transition dipole of the dye molecule. The excited dye fluoresces (at a wavelength somewhat longer than the wavelength of excitation). The fluorescence signal can be rooted through the polarizer. The intensity of detected light depends on the angle between the polarization direction of the polarizer and the emission transition dipole of the dye. In principle, one can use different schemes of placing the polarizing elements. In this work, we use a scheme with only one (linear) polarizer that polarizes both the incident and the fluorescent beams. The intensity of detected fluorescence signal is related to the director orientation provided the dye's transition dipoles are aligned along the director. If the polarization direction **P** of the incident light and the transition dipole are perpendicular, as in Figs.2 b and c, the fluorescence is practically zero. If the polarization **P** and the transition moment are parallel, the fluorescence is maximum, Fig.2d.
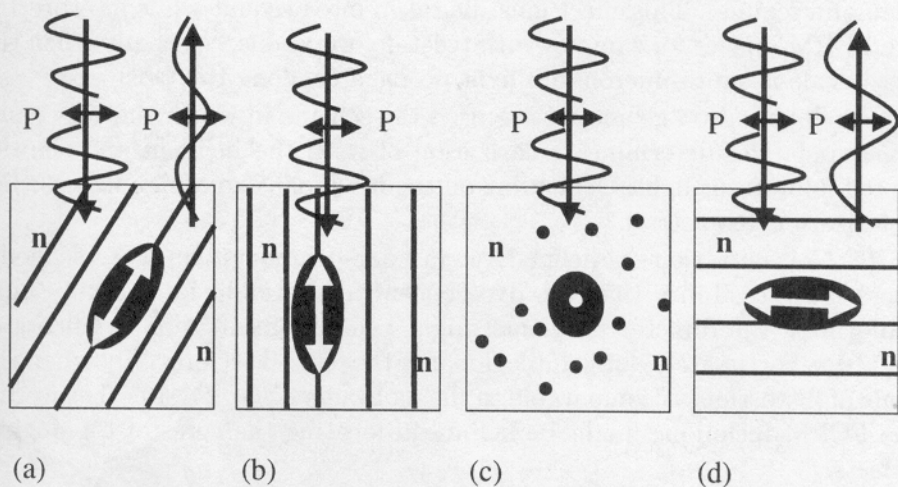

Figure 2. Principle of visualizing the director field in FCPM. The fluorescent molecule (black ellipsoid) is aligned by the director field (solid straight lines in part (a)). Polarized probing light excites the dye molecule that fluoresces. The efficiency of excitation depends on the angle between the transition moment of the dye molecule and the polarization of probing light. The efficiency is minimum for geometries (b) and (c), maximum for (d) and intermediate for (a).

More detailed account of FCPM, both theoretical and experimental, is given in the following sections. Here we list some specific requirements relevant to the FCPM imaging of the LC director field.

(1) Fluorescent probe. The probe should dissolve, align and fluoresce in the anisotropic host. Different materials (e.g., thermotropic vs. lyotropic LCs) would require different dyes. To study electro-optic phenomena, especially at DC fields, one might wish to avoid dyes of ionic nature as these would redistribute in the electric field; the intensity pattern might reflect the non-uniform concentration of the ionic dye rather than the director orientation. The concentration of dye and the intensity of light should be low enough to avoid light-induced director distortions in dye-doped liquid crystals [23].

(2) Optics of anisotropic medium. Focusing the laser beam in a birefringent medium is more complicated than in an isotropic medium since there are two propagating modes with different indices of refraction. To reduce the aberrations one can use a liquid crystal host with a low birefringence.

(3) Light absorption. Reducing the concentration of dye, the depth of scanning, and the thickness of the sample all help to mitigate this problem.

(4) Adiabatic following of polarization. The well-known effect in the optics of liquid crystals is that the polarization of both ordinary and extraordinary waves follows the local director in a twisted cell (the so-called Mauguin regime). This effect must be taken into account while interpreting the FCPM images for samples with twist deformations, especially when the twist scale is supra-micron and light propagates along the twist axis.

(5) Polarization geometry. We used the scheme in which the very same linear polarizer determines polarization of both the incident and the detected fluorescent light. Depending on the need, one can design many other polarization geometries.

(6) Concentration gradients. Even in a one-component anisotropic medium there is a possibility that the dye concentration would be spatially non-uniform as the director gradients might cause concentration gradients of the dyes. Fortunately, for soluble dopants the effect is strong only when the scale of distortions is comparable to the molecular scale [24]. In other words, the FCPM technique might be helpful in locating the cores of topological defects.

(7) Light scattering. Due to director fluctuations, light scattering in LCs is rather strong and leads to losses of intensity of both exciting and fluorescent light. Using LCs with small birefringence helps to reduce light scattering.

The estimation of radial and axial resolution for confocal imaging in birefringent medium is not as straightforward as in the case of isotropic liquid, as the volume of the voxel is obviously increased. Moreover, the fluorescing volume and resolution become dependent on spatial coordinates (especially in the case of spatially varying director field). Apparently, the best resolution of the reflective mode FCPM can be obtained in the close

vicinity of the entry plane of the exciting beam. The resolution is close to the estimates given above for the isotropic media, since the light does not propagate deeply into the birefringent volume. As the penetration inside the birefringent volume increases, the spatial defocusing of the ordinary and extraordinary modes can be estimated roughly as $\Delta z_{anis} \sim g\Delta nz/n_{ave}$, where n_{ave} is the average refractive index, z is the depth of scanning (penetration), and g is a coefficient of the order of unity (dependent on the sample orientation, NA of objective, and the director field). For a $20\,\mu m$ depth of focusing and $\Delta n/n_{ave} \sim 0.05$, the defocusing is of the order of $1\,\mu m$; the lower the birefringence Δn of the liquid crystal, the better.

3.4. THEORETICAL FOUNDATIONS OF CONFOCAL MICROSCOPY OF ORIENTATION PATTERNS

The FCPM signal is produced as a sequence of two processes: absorption and emission. Light absorption by an isolated dye molecule at the point with orientation Ω reads:

$$I_{abs} \propto I_0 \left(\mathbf{d}(\Omega)\cdot\mathbf{E}(\mathbf{r})\right)^2, \tag{19}$$

where I_0 is the intensity of excitation beam, $\mathbf{d}(\Omega)$ is the dipole moment of the absorption transition in the dye molecule with orientation Ω, $\mathbf{E}(\mathbf{r})$ is the electric field of irradiation, normalized for the unit intensity.

The effect of collective response of dye molecules in condensed media is described by two different approaches. The first approach considers the absorption as a result the interaction between a single molecule and the local electric field, $\mathbf{E}(\mathbf{r}) \to \mathbf{E_{loc}}(\mathbf{r})$ in Eq.(19). This approach was originally used to derive Lorentz-Lorenz formula for an isotropic medium and then was generalized for various anisotropic media (see e.g. [25] and references therein). The second approach is based on quantum calculation of macroscopic polarization and is effectively used in the theory of excitons [26]. In LCs this approach results in the effective dipole moment $\tilde{\mathbf{d}}(\Omega, \mathbf{n}(\mathbf{r}))$, $\mathbf{d}(\Omega) \to \tilde{\mathbf{d}}(\Omega, \mathbf{n}(\mathbf{r}))$ in Eq.(19) [27]. The latter approach is more convenient for our consideration, because it deals with the macroscopic electric field $\mathbf{E}(\mathbf{r})$.

The confocal setup of the microscope allows us to simplify the consideration of fluorescent emission. In FCPM the detector is small, and is positioned in the plane confocal with the point source. In this case the emission of the dye molecule that reaches the detector can be calculated using the reciprocity theorem [28]:

$$I_{em} \propto I_{abs} \left(\tilde{\mathbf{d}}'(\Omega', \mathbf{n}(\mathbf{r})) \cdot \mathbf{E}'(\mathbf{r})\right)^2, \tag{20}$$

where $\tilde{\mathbf{d}}'(\Omega',\mathbf{n}(\mathbf{r}))$ is the effective dipole moment of the emission transition, Ω' denotes the orientation of the dye molecule at the moment of emission, $\mathbf{E}'(\mathbf{r})$ is the electric field of irradiation, normalized for the unit source intensity. $\mathbf{E}'(\mathbf{r})$ is practically the same as $\mathbf{E}(\mathbf{r})$. The difference between $\mathbf{E}'(\mathbf{r})$ and $\mathbf{E}(\mathbf{r})$ is caused by two factors. First, the optical characteristics of the system may slightly differ on the absorption and fluorescence frequencies. Second, one can use different polarization schemes in the absorption and fluorescence paths. However, in our work we use the very same polarizer for both absorption and fluorescence paths in order to increase the FCPM sensitivity to the director orientation.

Averaging over orientations of the dye molecule and integrating over the spatial coordinates, we obtain the FCPM signal on the detector :

$$I_{FCPM} \propto I_0\, c_0\, Q \int \chi_{\alpha\beta,\gamma\xi}(\mathbf{r})\mathbf{E}_\alpha(\mathbf{r})\mathbf{E}_\beta(\mathbf{r})\mathbf{E}'_\gamma(\mathbf{r})\mathbf{E}'_\xi(\mathbf{r})d^3\mathbf{r}, \qquad (21)$$

where c_0 is the dye concentration, Q is the quantum yield of dye fluorescence, $\chi_{\alpha\beta,\gamma\xi}(\mathbf{r})$ is the fluorescence tensor, which is symmetrical with respect to permutation inside pairs of indices $(\alpha \leftrightarrow \beta,\ \gamma \leftrightarrow \xi)$ and reads:

$$\chi_{\alpha\beta,\gamma\xi}(\mathbf{r}) = \int \begin{array}{l} f(\Omega)G(\Omega,\Omega')\tilde{\mathbf{d}}_\alpha(\Omega,\mathbf{n}(\mathbf{r}))\tilde{\mathbf{d}}_\beta(\Omega,\mathbf{n}(\mathbf{r}))\times \\ \tilde{\mathbf{d}}'_\gamma(\Omega',\mathbf{n}(\mathbf{r}))\tilde{\mathbf{d}}'_\xi(\Omega'\mathbf{n}(\mathbf{r}))d\Omega d\Omega', \end{array} \qquad (22)$$

$$G(\Omega,\Omega') = \tau^{-1}\int_0^\infty G(\Omega,\Omega',t)\exp\{-t/\tau\}dt.$$

Here $f(\Omega)$ is the orientational distribution function for a dye molecule, τ is the lifetime of the dye excited state, $G(\Omega,\Omega',t)$ is the orientational autocorrelation function for a dye molecule, that determines the probability of molecular orientation Ω' at the moment t if the initial orientation is Ω. If $\tau \ll \tau_D$, where $\tau_D \sim 10^{-8}s$ is the characteristic time of rotational diffusion, then $G(\Omega,\Omega') \to \delta(\Omega-\Omega')$. In other words, the orientation of the dye molecule at the moment of emission is practically the same as at the moment of absorption.

In the opposite limit $\tau \gg \tau_D$, the dye molecule has enough time to forget the initial orientation and its orientation at the moment of emission is determined by the orientational distribution function $f(\Omega')$, i.e., $G(\Omega,\Omega') \to f(\Omega')$. In this case, the tensor $\chi_{\alpha\beta,\gamma\xi}(\mathbf{r})$ in Eq.(22) splits into the absorption tensor $\kappa_{\alpha\beta}(\mathbf{r})$ and the emission tensor $\mu_{\gamma\xi}(\mathbf{r})$:

$$\chi_{\alpha\beta,\gamma\xi}(\mathbf{r}) = \kappa_{\alpha\beta}(\mathbf{r})\,\mu_{\gamma\xi}(\mathbf{r}) , \qquad (23)$$

where

$$\kappa_{\alpha\beta}(\mathbf{r}) = \int f(\Omega)\tilde{\mathbf{d}}_\alpha(\Omega,\mathbf{n}(\mathbf{r}))\tilde{\mathbf{d}}_\beta(\Omega,\mathbf{n}(\mathbf{r}))d\Omega,$$

$$\mu_{\alpha\beta}(\mathbf{r}) = \int f(\Omega')\tilde{\mathbf{d}}'_{\gamma}(\Omega', \mathbf{n}(\mathbf{r}))\tilde{\mathbf{d}}'_{\xi}(\Omega', \mathbf{n}(\mathbf{r}))d\Omega'.$$

Most of the LCs are locally uniaxial media with no polar order. In these media, $\chi_{\alpha\beta,\gamma\xi}(\mathbf{r})$ is of the form

$$\chi_{\alpha\beta,\gamma\xi}(\mathbf{r}) = \chi_1\delta_{\alpha\beta}\delta_{\gamma\xi} + \chi'_1\left(\delta_{\alpha\gamma}\delta_{\beta\xi} + \delta_{\alpha\xi}\delta_{\gamma\beta}\right) + \chi_2 n_\gamma n_\xi \delta_{\alpha\beta} + \bar{\chi}_2 n_\alpha n_\beta \delta_{\gamma\xi}$$
$$+\chi'_2\left(n_\alpha n_\xi \delta_{\gamma\beta} + n_\beta n_\xi \delta_{\alpha\gamma} + n_\gamma n_\alpha \delta_{\beta\xi} + n_\gamma n_\beta \delta_{\alpha\xi}\right) + \chi_3 n_\alpha n_\beta n_\gamma n_\xi, \quad (24)$$

where χ_i are the material constants, which depend on the orientation of absorption and emission dipole moments with respect to the molecular axes and on the orientational order of dye molecules. If $\tau \gg \tau_D$, then $\chi'_1, \chi'_2 \to 0$ and $\chi_1 = \kappa_\perp \mu_\perp$, $\chi_2 = \kappa_\perp\left(\mu_\| - \mu_\perp\right)$, $\bar{\chi}_2 = \left(\kappa_\| - \kappa_\perp\right)\mu_\perp$, $\chi_3 = \left(\kappa_\| - \kappa_\perp\right)\left(\mu_\| - \mu_\perp\right)$, where $\|$ and $\perp$ denote tensor components, respectively parallel and perpendicular to the director.

To view the director in calamitic LCs, it is beneficial to use dye molecules in which the absorption and emission dipole moments are both along the long molecular axis. In this case, as follows from formulas above, the anisotropy of the fluorescence tensor $\chi_{\alpha\beta,\gamma\xi}(\mathbf{r})$ is significantly larger than linear dichroism caused by the dye molecules. The dye molecules of this type provide the strongest sensitivity of FCPM to the director orientation.

4. Experimental set up and materials

4.1. EXPERIMENTAL SET UP

Figure 3 shows the FCPM set up assembled on the base of Olympus Fluoview BX-50 confocal microscope, modified by a rotating linear polarizer $\mathbf{P}$. The polarizer determines polarization of the excitation beam, $\mathbf{P_e}\|\mathbf{P}$, and polarization of the detected fluorescent light, $\mathbf{P_f}\|\mathbf{P}$. The excitation beam (488 nm, Ar laser) is focused by an objective into a small ($< 1\,\mu m^3$) volume in the cell. The fluorescent light from this volume is detected by a photomultiplier tube (PMT1) in the spectral region 510-550 nm selected by interference filters (channel #1). A pinhole discriminates against the regions above and below the selected volume [18]. The pinhole size is adjusted depending on magnification and numerical aperture of the objective. For example, for a $60\times$ objective with NA = 1.4, the pinhole diameter is set at $100\,\mu m$. The focused beam scans the sample both in the horizontal plane, located at a fixed depth z, and in the vertical plane. The intensity of fluorescence as the function of coordinates is measured and stored in the computer memory. Each horizontal scan produces a thin "optical slice" with thickness determined by the resolution of FCPM. The beam power is small, $\approx 120\,nW$, to avoid light-induced reorientation of the dye-doped LC.

Besides the immersion-oil objective with $60\times$, NA = 1.4, we also used dry objective $40\times$ with NA = 0.6.
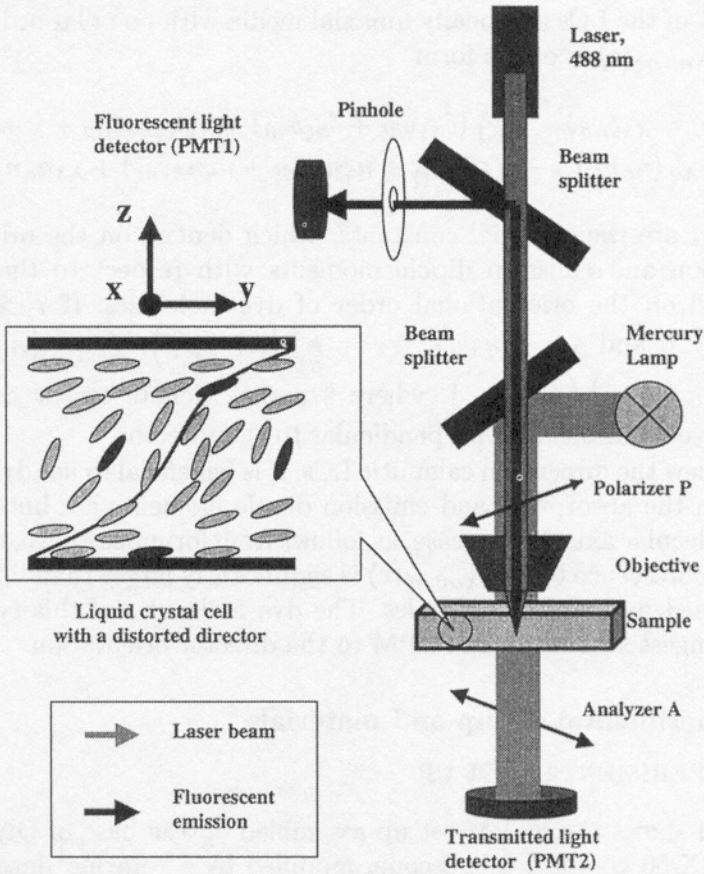

Figure 3. Experimental FCPM set-up used in this work.

Simultaneously with the FCPM image, a standard polarizing-microscope texture of the same sample is recorded by measuring the intensity of light that passes through the polarizer P, sample, and a crossed analyzer A, Fig.3. The intensity of transmitted light is detected by PMT2, channel #2. Note that the wide view polarizing microscope textures are obtained in the transmission mode while the FCPM textures are obtained in the reflection mode.

4.2. LIQUID CRYSTAL MATERIALS AND FLUORESCENT PROBES.

We study both nematic and cholesteric materials. To obtain a cholesteric LC, a small amount of chiral dopant CB-15 is added to the nematic mix-

tures ZLI-3412 and ZLI-2806 (all materials purchased from EM Industries). The LC materials have low birefringence to mitigate the defocusing effect: $\Delta n \approx 0.078$ for ZLI-3412 and $\Delta n \approx 0.044$ for ZLI-2806. We also used the nematic mixture E7 with $\Delta n \approx 0.224$ in some of the experiments on cholesteric diffraction gratings. Since resolution gets worse according to the estimate $\Delta z_{anis} \sim g\Delta nz/n_{ave}$, only thin (less than $10\,\mu m$) cells were used with E7. Keeping the specimens thin also helps to prevent abberations caused by a mismatch between the refractive index of the cover glass and the refractive index of the specimen [29]. Although the average refractive indices of the chosen LCs match the refractive index of cover glass reasonably well, we still performed all the experiments in cells thinner than $30\,\mu m$.

N,N'-Bis(2,5-di-tert-butylphenyl)-3,4,9,10-perylenedicarboximide (BTBP)

(a)

Rhodamine 6G, perchlorate

(b)
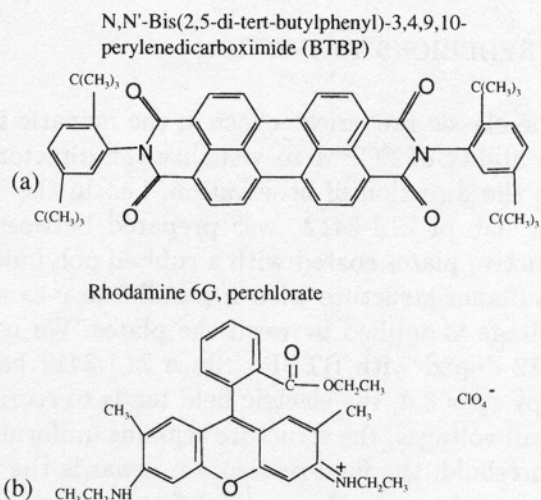
Figure 4. Molecular structures of fluorescent probes used for FCPM imaging of LCs: (a) BTBP and (b) Rhodamine 6G perchlorate.

For FCPM observations all the LC materials are doped with $\sim 0.01\%$ (by weight) of fluorescent dyes that have molecules of anisometric shape, Fig.4. We used two dyes: n,n'-bis(2,5-di-tert-butylphenyl)-3,4,9,10-perylenedicarboximide (BTBP) and Rhodamine 6G perchlorate, purchased from Molecular Probes. BTBP is especially effective for imaging director patterns under the applied electric fields since it contains no ionic groups. BTBP shows maximum absorption for light polarized along the long axis of the molecule and minimum absorption for light polarized in perpendicular directions [30]. Fluorescence light is polarized predominantly along the long axis of the molecule. Both dyes strongly fluoresce when excited by Ar-laser at 488 nm and have a rather large Stokes shift, 30 nm - 60 nm. The concentra-

tions of fluorescent probes are too small to affect the LC structure, but sufficiently high to produce a strong fluorescence signal.

To verify if the dye is well oriented, we prepared a nematic cell (ZLI-3412 doped with BTBP) with **n** aligned uniformly in the plane of the cell, and measured the intensity of fluorescence (averaged over the cell area) as the function of the angle between **P** and **n**. The intensity of fluorescence is maximum when **P**∥**n** and minimum when **P**⊥**n**, the ratio being 7.5, which indicates that the dye molecules are well oriented along **n**. The strong orientation dependence of measured fluorescence signal allows one to decipher the 3D orientation pattern from the FCPM observations.

5. Results and Discussion

5.1. FCPM OF FREDERICKS TRANSITION

We start with the classic Fredericks effect in the nematic liquid crystal to demonstrate the ability of FCPM to visualize the director pattern in the plane parallel to the direction of observation, i.e., in the "vertical" plane [5]. The nematic slab of ZLI-3412 was prepared between two transparent electro-conductive plates coated with a rubbed polyimide PI-2555. The polyimide sets a planar structure with **n** parallel to y-axis, Fig.5 on page 263. The AC voltage is applied between the plates. We used the nematic material ZLI-3412 doped with BTBP. Since ZLI-3412 has a positive dielectric anisotropy $\varepsilon_a = 3.4$, the electric field tends to reorient the director vertically. At small voltages, the structure remains uniform, Fig. 5a. Above a well-defined threshold, the field reorients **n** towards the z-axis [22]. The maximum deviation of **n** is in the middle of the cell, as predicted by the theory [22], Fig.5a.

To describe the distortions, we parameterize the director **n** through the polar angle θ and the azimuthal angle φ: $n_x = \sin\theta\sin\varphi$, $n_y = \sin\theta\cos\varphi$, $n_z = \cos\theta$. The dependence of θ on the vertical coordinate z for different applied voltages is shown in Fig.5b. The plot was obtained by computer simulations of the director within the frame of Frank-Oseen theory, taking into account inhomogeneous electric field, as explained in Ch.2. The azimuthal angle $\varphi = 0°$ remains constant. The beginning of the Fredericks transition is clearly manifested in the FCPM texture by a reduced intensity of light emitted from the middle of the cell. As the field increases, both the amplitude of director reorientation and the thickness of reoriented zone increase, Fig. 5a. Close to the substrates of the cell (that have no fluorescent dyes and appear black) the image is blurred due to limited resolution of the confocal imaging system.

5.2. FCPM OF TWISTED NEMATIC CELL

Now we test the capabilities of FCPM to image twisted director configurations, taking as an example the twisted nematic (TN) cell. The TN cell was prepared as described above for the Fredericks experiment, with that difference that the directions of rubbing at the two substrates were perpendicular to each other. The cell was filled with the nematic mixture ZLI-3412.

The twist axis is parallel to the optical axis of the microscope. The specific feature is that for light propagation along the twist axis, the polarization of both ordinary and extraordinary waves can follow the local director when the pitch p of the helicoidal twist is much larger than the wavelength λ of light (the so-called Mauguin regime) [1, 31]. We define the Mauguin number

$$\text{Mau} = \frac{p \Delta n}{2\lambda}, \tag{25}$$

so that the Mauguin condition reads: Mau $\gg 1$. For a TN cell, $p = 4d$, where d is the cell thickness. With $d = 20\,\mu m$, the Mauguin condition is satisfied.

At zero voltage, the polar angle $\theta = 90°$ is constant throughout the cell, while the azimuthal angle φ is a linear function of the z - coordinate, Fig.6c on page 264. We image vertical cross-sections of the TN cell in the regime of ordinary wave excitation ($\mathbf{P} \perp \mathbf{n}$ at the irradiated top plate, Fig.6a), and in the regime of extraordinary wave excitation ($\mathbf{P} \| \mathbf{n}$ at the top plate, Fig.6b). The fluorescence signal is much stronger in the case of extraordinary wave excitation, Fig.6b, since the light polarization follows the local director. The fluorescence signal is practically uniform in both horizontal and vertical scans of the cell, Figs. 6a and 6b. In other words, the macroscopic 90° - twist is not visualized because of the Mauguin effect.

When the applied voltage exceeds the threshold of Fredericks transition in the TN cell, the director reorients. Both functions $\theta(z)$ and $\varphi(z)$ change, as the computer simulations based on the Frank-Oseen theory in Fig.6e demonstrate. In the regions with small θ, the effective birefringence is reduced. For example, our estimates show that in the middle plane of the cell, the effective birefringence is 0.003, well below its original value 0.078 at zero voltage. Smaller birefringence means that the Mauguin number is reduced, see Eq.(25). The Mauguin condition is not satisfied anymore and light polarization does not follow the director twist exactly. The last feature allows one to visualize the orientation of dye in the TN cell, at least partially.

The vertical (x, z) cross-sections of the cell at different applied voltages are shown in Fig.6d; $\mathbf{P} \perp \mathbf{n}$ at the top substrate. At voltages $3V$ and higher, the fluorescence signal is stronger near the bottom substrate, where $\mathbf{n} \| \mathbf{P}$.

For better understanding, compare Fig.6d with Figs. 6a and 6b. At very high voltages $> 12\,V$, the director is vertical, $\theta \approx 0$, almost everywhere in the cell. Therefore $\mathbf{P} \perp \mathbf{n}$, and the fluorescence signal is weak. The experiment with TN cell shows that the director twist in the direction of observation can be visualized by FCPM if the Mauguin number is not too large.

The textures in Fig.6 were obtained with the $40\times$ objective, NA $= 0.6$. Using objectives with a higher NA makes the observations of the twisted director easier since the focused laser beam forms a wider cone; the eigen modes for oblique incidence are not linearly polarized even when Mau $\gg 1$ [32]. Of course, small birefringence of the LC material also helps, as it reduces both the Mauguin number (25) and the defocusing effects.

5.3. THE FCPM IMAGING OF BASIC CHOLESTERIC TEXTURES.

The director configuration of the cholesteric LC in a confined volume depends on twisting power of molecular interactions, boundary conditions, and applied external fields. The resulting 3D patterns are hard to decipher since the standard PM yields images integrated over the z - direction. The FCPM technique is capable of a better insight. Below we discuss different regimes of FCPM imaging in cholesteric samples, specified by the Mauguin number and the type of textures.

(a) **Planar cholesteric texture,** Mau ≈ 0.8.

We first consider the simplest case of a planar cholesteric texture. The eigen modes in general are two elliptically polarized waves whose principal axes remain aligned with the principal axes of the dielectric tensor [1, 31]. The ellipticity of the eigen modes depends on the pitch/wavelength ratio p/λ, or, equivalently, the Mauguin number defined in Eq.(25).

We use a cholesteric mixture of ZLI-3412 and CB-15 doped with the fluorescent dye BTBP to visualize the director pattern in a planar cholesteric texture with a uniform director twist around the normal to the slab (Fig.7 on page 264). The concentration of CB-15 was chosen to produce a relatively short helical pitch $p = 10\,\mu m$. In contrast to the experiment on weakly twisted cell described in section 5.2., this time the Mauguin condition is not satisfied since with $p = 10\,\mu m$, $\Delta n = 0.078$, $\lambda = 0.5\,\mu m$ one obtains Mau ≈ 0.8 from Eq.(25). Propagating light decomposes into two elliptically polarized eigen modes with ellipticity close to unity [31]. Their interference produces a wave with polarization state close to the linear polarization of the incident light. Director twist around the vertical axis is clearly visualized in the FCPM texture, Fig.7.

(b) **Oily streaks and dislocations,** Mau ≈ 0.4.

The planar cholesteric texture is often accompanied by defects of which

the most common are oily streaks and dislocations in the systems of layers [33, 34, 35]. For $p = 5\,\mu m$ used in this experiment, Mau ≈ 0.4. As it can be seen from Figs. 8 and 9, FCPM readily visualizes both oily streaks and dislocations. The FCPM textures confirm the basic model of an oily streak as a pair of parallel disclinations of strength $+1/2$ with a wall defect between them [33, 36, 37]. The cholesteric layers either interrupt at this wall, or continuously reorient by 180^0 around the cores of the two disclinations. Most importantly, the textures clearly reveal that the two disclinations of strength $+1/2$ at the base of the oily streak are of the λ type, according to the Kleman-Friedel terminology [33]. In the λ-disclinations, the director is oriented along the core of the disclination, which is thus singular in the field of the helical axis but not in the director field. Dislocations can also be considered as disclinations in the field of the helical axis [33, 34]. All the defect lines in Figs. 8 and 9 are of the λ type. We stress that the FCPM textures in Figs. 8c and 9b show the cross-sections of the disclination lines; since the lines run parallel to the substrates of the cell, their type and location along the z-axis would be hard to identify in the usual PM.
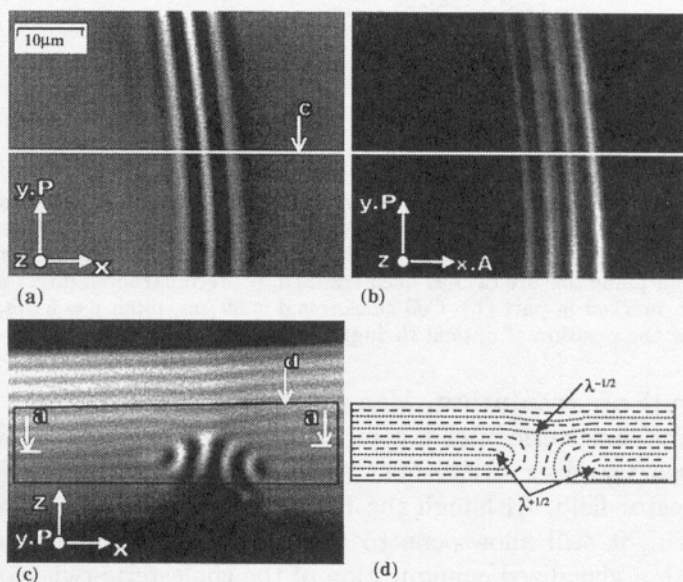
Figure 8.   An oily streak in a cholesteric cell of thickness $d = 30\,\mu m$, cholesteric pitch $p = 5\,\mu m$: (a) FCPM texture in the horizontal (x, y) plane of the cell; (b) PM texture of the same region as in (a); (c) FCPM texture of the vertical cross section of the cell along the line marked as "c" in (a); (d) schematic director field near the center of the oily streak. Bars and dots in (d) represent the director parallel and perpendicular to the plane of the figure, respectively. Bars marked "a" in (c) show the depth at which the texture (a) was scanned.
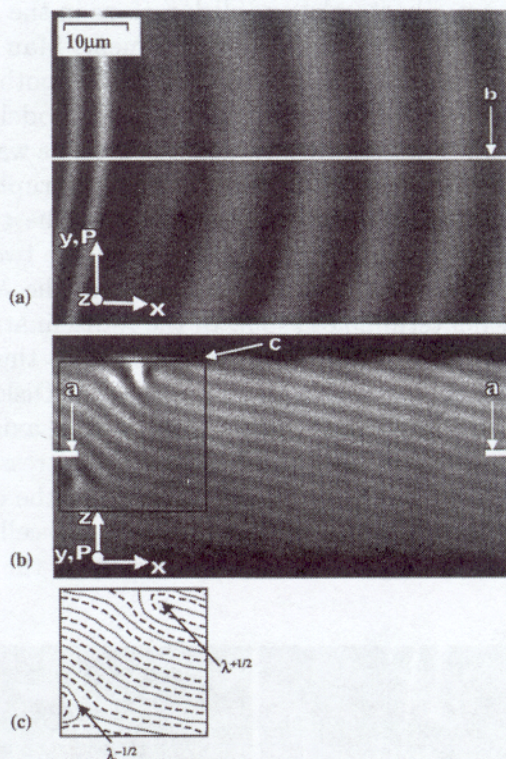
Figure 9. FCPM images of a cholesteric LC cell with oblique orientation of layers and dislocations: (a) optical section in the plane of the cell; label "b" shows the line of vertical cross-section presented in (b); alternatively, bars marked "a" in part (b) show the depth at which the in-plane texture (a) has been scanned; (c) reconstructed director field of the square region marked in part (b). Cell thickness $d = 30 \, \mu m$, pitch $p = 5 \, \mu m$. Labels "b" and "a" show the position of optical slicing.

(c) Limit of resolution, Mau ≈ 0.08.

When the cholesteric pitch is comparable or smaller than the wavelength of light used for observation, one reaches the limit of FCPM resolution for the director field. Although the FCPM is not capable of resolving the director field, it still allows one to obtain a "coarse-grained" cholesteric texture with a visualized configuration of the cholesteric twist axis **m** that is perpendicular to the director, **m⊥n**, see Fig.10.

The short-pitch ($p = 1 \, \mu m$) mixtures of ZLI-3412 and CB-15 were doped with the fluorescent BTBP. The cells of thickness $30 \, \mu m$ were treated for tangential alignment of the director. The Mauguin number for the cell is Mau ≈ 0.08, the ellipticity of eigen modes is close to unity, i.e., the normal modes are almost circularly polarized with the opposite sense of handedness. The FCPM and PM images of oily streaks in the cell are shown in
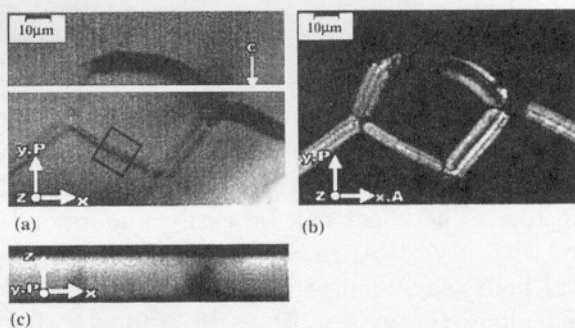
(a)

(b)

(c)

Figure 10. An oily streak in a tightly twisted cholesteric with the small pitch $p = 1\,\mu m$: (a) FCPM slice parallel to the plane of the cell; (b) the corresponding PM image of the same region; (c) FCPM texture of the vertical cross-section of the cell. Cell thickness $d = 20\,\mu m$.
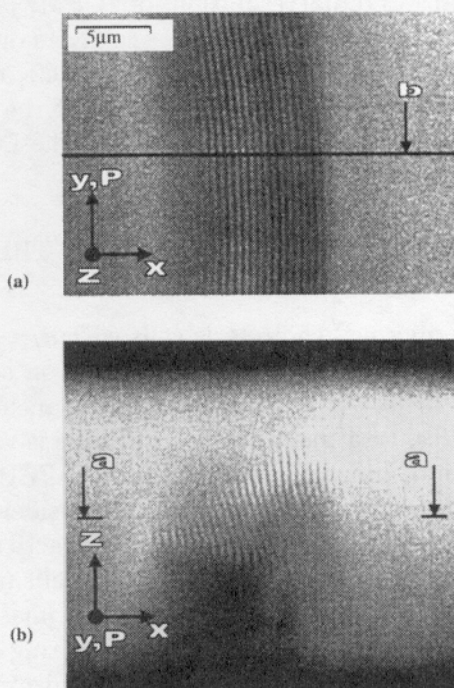

(a)

(b)

Figure 11. Enlarged FCPM image of a part of the cholesteric oily streak marked by a rectangle in Fig.10(a): (a) in-plane image taken at the depth of scanning $\sim 8\,\mu m$; (b) vertical cross-section.

Figs. 10 and 11 (objective $60\times$, NA $= 1.4$). Figure 11 is the zoomed image of the oily streak marked by a square in Fig.10.

The helical twist of the director in the planar texture is not visible in Fig.10, since the pitch is too small. However, the regions where the cholesteric layers are parallel to the plates are distinguishable from the regions where the layers are tilted or vertical, as in the neighborhood of the oily streaks, Fig.10c. The effect can be easily understood by comparing a planar texture with a vertical $\mathbf{m} = (0,0,1)$ and a "fingerprint" texture with a horizontal helix, say, along the axis y, $\mathbf{m} = (0,1,0)$. Suppose that light is polarized along the axis y, $\mathbf{P} = (0,P,0)$. In the first case, the fluorescent molecules, following the director, are always in the horizontal (x,y) planes. The angle between the polarization $\mathbf{P}$ and the long axes of the dye molecules is periodically changing from 0 to $\pi/2$ and back to 0, with the small period $p/2$. In the second case, $\mathbf{n}$ is always perpendicular to $\mathbf{P}$ and thus the intensity of fluorescence is lower than in the first case. Dark portions of oily streaks in Fig.10a represent the geometry of the second case.

Figure 11 with a magnified image of the oily streak demonstrates some difference in the axial and radial resolutions of FCPM. The cholesteric layers oriented vertically are resolved better than the layers oriented horizontally. The radial resolution in the experiment is about $0.2\,\mu m$ (at least close to the top boundary) while the axial resolution is of the order of $1\,\mu m$ and worsens as the scanning beam moves deeper into the LC layer.

5.4. FIELD-INDUCED CHOLESTERIC STRIPES IN THIN CELLS WITH PLANAR BOUNDARY CONDITIONS

Relatively thin (few microns) cholesteric cells with $d/p \sim 1$ show especially rich variety of director patterns since at the micron scale all the factors (chirality, elasticity, dielectric torques and surface anchoring) are in direct competition. Analytical treatment of these patterns is very difficult. This is why the combination of computer simulations and FCPM becomes an efficient tool. In the following two subsections we consider how the two techniques are combined to clarify the structures of practical interest, namely, one-dimensional periodic director patterns in flat cells under external field. These periodic patterns are diffraction gratings of phase type that can be used in a variety of applications, e.g., in beam steering devices [39].

We used E7 with a strong positive dielectric anisotropy ($\varepsilon_a = 13.8$) as the nematic host. E7 was doped with the chiral dopant CB15 to obtain cholesterics with the pitch in the range $5-20\,\mu m$. BTBP was added to the cholesteric mixture for the FCPM studies. The cells with planar anchoring were assembled from two glasses coated with transparent ITO electrodes

and a polyimide PI-2555 as an alignment layer. Unidirectional buffing of the alignment layer sets planar orientation with a small pretilt angle. The directions of rubbing at the bounding plates of assembled cells were anti-parallel to each other. The pretilt angle β measured by the magnetic null method at the PI-2555 and E7 interface is small, $\beta = 1.5 - 2°$. The polar anchoring coefficient W_p is of the order of 10^{-4} J/m^2 [38].

In zero field the texture is uniformly planar. A very strong AC voltage ($> 5V$) induces the homeotropic texture. At intermediate voltages, there are two basic kinds of the in-plane modulated director patterns, called the "parallel stripes" and the "perpendicular stripes" (Fig.12), see Refs.[40, 20]. The parallel stripes appear by nucleation. They nucleate near spacers and other defects as circular domains and then elongate and propagate along the rub direction filling the available space. The perpendicular, or "developable," stripes appear simultaneously all over the domain. These modulations develop by enhancing the optical contrast rather than by nucleation and propagation in space.
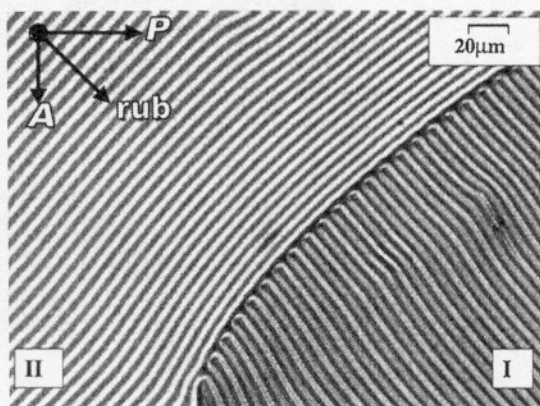

Figure 12. Polarizing microscope texture of parallel (I) and perpendicular (II) stripes in a cholesteric cell with planar boundary conditions. The arrows show the rub direction and orientation of the polarizer and analyzer.

(I) The parallel stripes. Computer simulations reveal two possible structures for the parallel stripes. We call them the "O" structure, Fig.13, and the "snake" structure, Fig.14. In both cases, the director configurations in the middle of the cell are similar to the ideal cholesteric helicoid with the periodicity $p/2$. However, surface interactions break the symmetry between two adjacent regions of the thickness $p/2$, so that the real periodicity doubles and becomes approximately equal to the pitch [39]. The difference in

the calculated free energies of the two structures is rather small (less than 5%) to give a clear preference to either one of them.
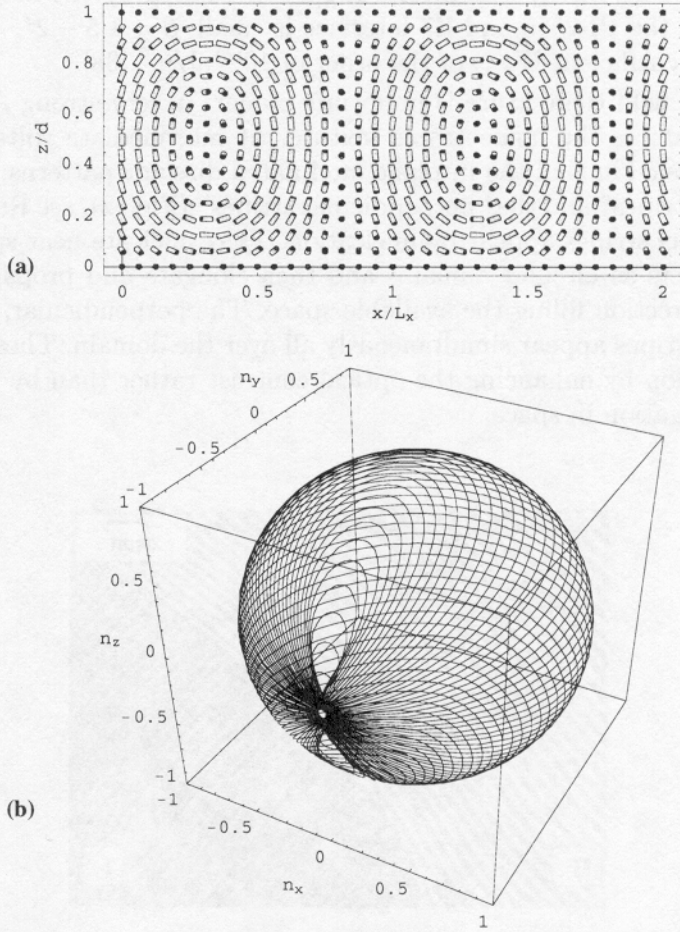

Figure 13.   Computer simulated "O" structure of the parallel stripes (I) in a cholesteric cell with a planar anchoring: (a) director field over two periods of the structure; (b) S^2 representation. Parameters of simulations: Frank elastic constants $K_{11} = 6.4, K_{22} = 3, K_{33} = 10$ and $K_{24}=0$ (in pN), $W_p d/K_{33} = 40, W_a d/K_{33} = 20,$ $\theta_p = 2°, \varepsilon_a = 13.8, \varepsilon_\perp = 5.2$, applied voltage $1.6V$. The stripes are parallel to the rubbing direction (y-axis).

The FCPM images of the parallel stripes are shown in Fig.15a,b on page 265, for a mixture with $p \approx 3.5\,\mu m$, in a cell of thickness $d \approx 4\,\mu m$. The Mauguin number Mau ≈ 0.8 is sufficiently small to prevent the Mauguin effect; the polarization of incident light is parallel to the stripes. Symmetry of the vertical cross-section of FCPM image, Fig.15b, is similar to the "O"
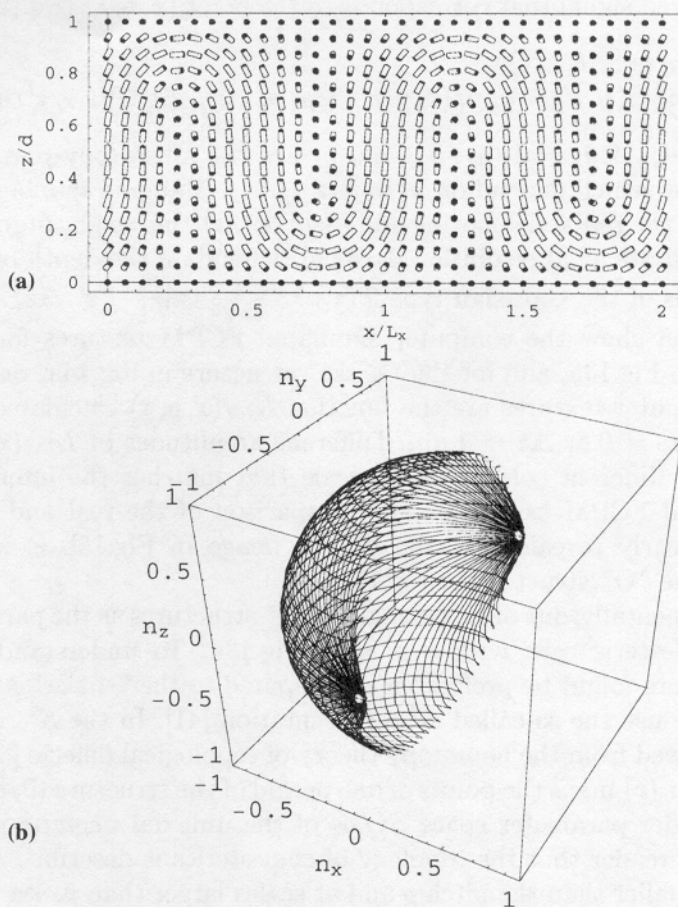
Figure 14. Computer simulated "snake" structure of the parallel stripes (I) in a cholesteric cell with a planar anchoring: (a) director field over two periods of the structure; (b) S^2 representation. Parameters of simulations the same as in Fig.13. The stripes are parallel to the rubbing direction(y-axis).

structure in Fig.13a. To make the identification unambiguous, we simulate the FCPM textures by applying Eq.(21) to the computer-generated director patterns in Fig.13a and 14a. We assume that $\tau \gg \tau_D$, so that Eq.(23) holds. Furthermore, we assume that the absorption tensor $\kappa_{\alpha\beta}(\mathbf{r})$ and the emission tensor $\mu_{\gamma\xi}(\mathbf{r})$ have the same relative anisotropy $\left(\kappa_{\parallel}/\kappa_{\perp} = \mu_{\parallel}/\mu_{\perp}\right)$, and that the optical characteristics of the cell are the same at the absorption and emission wavelengths. These assumptions reduce the number of unknown fitting parameters but do not alter the qualitative features of the analysis.

The measured signal that corresponds to the point (x, y, z) (Eq.(21)) reads:

$$I_{CM}(x, y, z) \propto I_0\, c_0\, Q \times$$
$$\int [g_x\, n_x^2(x, y, z') + g_y\, n_y^2(x, y, z') + g_z\, n_z^2(x, y, z')]^2 T(z - z')\, dz', \quad (26)$$

where $g_x + g_y + g_z = 1$; g_x, g_y, and g_z are the anisotropy parameters of fluorescence, which depend on $\kappa_\parallel/\kappa_\perp = \mu_\parallel/\mu_\perp$, Mauguin number and NA. We neglect the radial defocusing and assume that the weight function $T(z')$ describing finite axial resolution does not depend on the depth of the focal plane and is of the Gaussian type $T(z') = \frac{1}{\Delta z \sqrt{\pi}} \exp\left[-(z'/\Delta z)^2\right]$. Figures 15c and 15d show the computer simulated FCPM textures for the "O" structure in Fig.13a, and for the "snake" structure in Fig.14a, respectively. These computer textures are the function $I_{CM}(x, y, z)$ calculated for $g_x = g_z = 0.2$, $g_y = 0.6$, $\Delta z = 1\,\mu m$. Different amplitudes of $I_{CM}(x, y, z)$ are labelled by different color, using a scale that matches the intensity-color scale in real FCPM experiments. Comparison of the real and computer textures clearly reveals that the FCPM image in Fig.15b is indeed the image of the "O" structure in Fig.13a.

Experimentally, one observes mainly "O" structures as the parallel stripes in the cholesteric cells with $d/p \sim 1$, Fig.13a. To understand why the "O" structure might be preferable as compared to the "snake" structure in Fig.14a, we use the so-called S^2 representation [41]. In the S^2 representation, borrowed from the homotopy theory of topological defects [33], the director field $\mathbf{n}(\mathbf{r})$ maps the points of one period of the structure $(0, L_x) \times (0, d)$ into the order parameter space S^2/Z_2 of the uniaxial *nematic* phase. We remind the reader that the topology of cholesterics is described differently at scales smaller than the pitch p and at scales larger than p, see the recent review [34] and references therein. For the scales of deformations smaller than p, topological features can be assumed to be the same as for the uniaxial nematic phase. In the notation S^2/Z_2, S^2 stands for a sphere of a unit radius. Each point of the sphere corresponds to a different orientation of the director $\mathbf{n}$. Since $\mathbf{n} \equiv -\mathbf{n}$, any two diametrically opposite points at S^2 describe indistinguishable states. Therefore, the order parameter space is the unit sphere S^2 factored by a subgroup Z_2, which is the group of two integers 0 and 1, isomorphic to the inversion group.

To obtain the S^2 representations of the computer-simulated director patterns, we scanned the area $(0, L_x) \times (0, d)$ of real space by a set of lines parallel to the z-axis and located at different $x = const$. The mapping $\mathbf{n}(\mathbf{r})$ of each linear scan produces a curve on the unit sphere S^2. Figures 13b and 14b are the S^2 representations of the "O" and "snake" director patterns in Fig.13a and Fig.14a, respectively. For the comparative analysis, it is also important to imagine how an ideal planar state threaded by linear scans along the twist axis z would look in the S^2 presentation. If the director

twists by π from plate to plate (the first Grandjean zone, $d/p \approx 1/2$), it will be a half of an equatorial circle at the sphere S^2. If the director twists by 2π (the second Grandjean zone, $d/p \approx 1$), it will be the whole equatorial circle on S^2. S^2 representations of "O" and "snake" structures are different. In the "O" structure, Fig.13b, all curves start and end at the same point of S^2, whereas in the "snake" structure, Fig.14b, the curves have their ends at the two diametrically opposite points of S^2. The preference of either structure is determined whether the initial zero-field planar structure corresponds to the odd or even Grandjean zone. For $d/p \approx 1$ (the second Grandjean zone), the zero-field planar structure corresponds to the equatorial circle at S^2. The "O" structure can coexist with this planar structure as an isolated finger. Each isolated finger can be considered as a part of the structure shown in Fig.13a that spans between the centers of the adjacent "O" patterns, from $x/L_x = 0.3$ to $x/L_x = 1.3$. As easy to see, the edges of the finger at $x/L_x = 0.3$ and $x/L_x = 1.3$ can be continued by a planar structure with a 2π director twist along the z-axis. This matching between the planar texture and the cholesteric fingers is clearly revealed by the FCPM texture in Fig.15b. On the other hand, the energy cost of matching the "snake" structure with the 2π director twist of the planar structure $d/p \approx 1$ is much higher, since either a half-integer disclination, or some other defect should be created to compensate for the difference in the number of π-twists. These features might explain why the "O" structures are preferable in the experimental specimens.

(II) The perpendicular stripes. Figure 16 shows computer simulations of the stripes that are perpendicular to the rubbing direction (axis x). The S^2 representation reminds a stretched equatorial ring, which represents the planar state $d/p \approx 1$, Fig.16b. Thus the perpendicular stripes can continuously develop from the planar state through a barrier-free dielectric instability similar to the Helfrich – Hurault undulations in multi-layered ($d/p \gg 1$) systems. The real and computer-simulated FCPM images of these "developable" perpendicular stripes are shown in Fig.17 on page 266, for a sample with $p \approx 10\,\mu m$ and $p/d \approx 1$. The Mauguin number Mau ≈ 2.2 is rather large which might explain the mismatch in the shape of the experimental and simulated FCPM images; what is clear, however, is that the image asymmetry is attributed to the non-zero pretilt angle at the substrates.

5.5. CHOLESTERIC STRIPES IN THIN CELLS WITH HOMEOTROPIC BOUNDARY CONDITIONS.

The homeotropic cells can contain in-plane modulated director patterns even when there is no external field. The homeotropic boundary conditions are incompatible with the helical structure and tend to unwind the
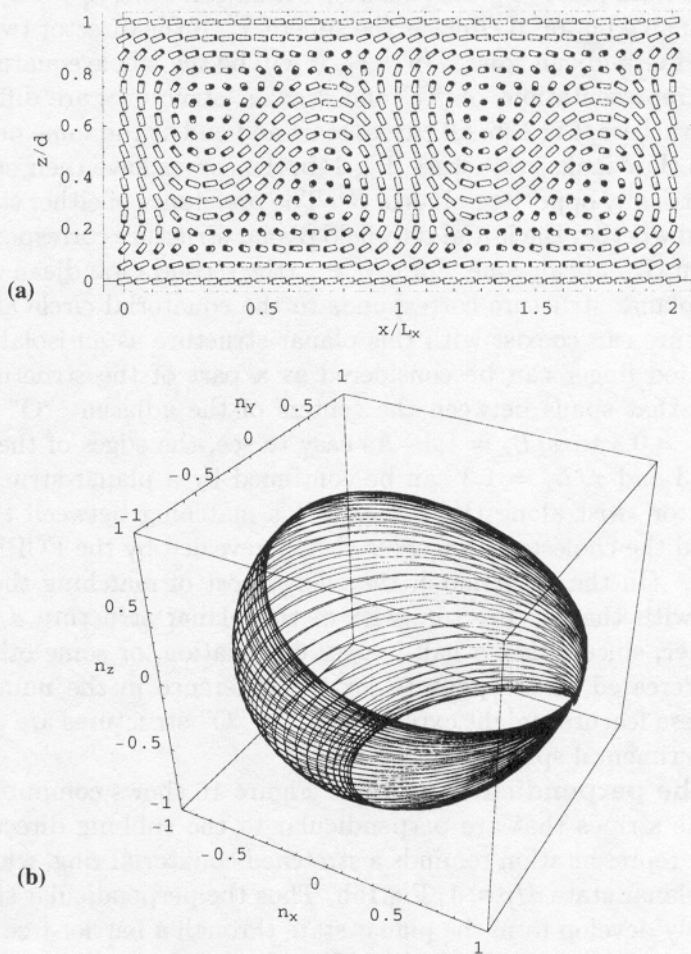
Figure 16. Computer simulated perpendicular stripes (II) in a cholesteric cell with planar anchoring: (a) director field over two periods of the structure; (b) S^2 representation. Parameters of simulations are the same as in Fig.13, except the applied voltage is $1.9V$. The rubbing direction is along the x axis (perpendicular to the stripes).

cholesteric. Balance of surface anchoring and bulk chirality leads to a variety of director configurations, see, for example, [43]. An apparent tentative parameter to characterize this balance is the ratio of the cell thickness d to the natural cholesteric pitch p: $C = d/p$. In thin cells with $d/p < C_c \sim 1$, where C_c is some critical number that depends on the anchoring strength and elastic constants, one finds homeotropic untwisted textures. An applied electric field increases or decreases C_c, depending on the sign of the dielectric anisotropy. If $d/p > C_c$, several in-plane modulated structures exist.

These structures have been classified in [42] on the basis of PM studies and computer simulations of isolated stripes (fingers). Identification of these cholesteric fingers by ordinary PM is rather difficult since different director configurations might yield similar PM textures.

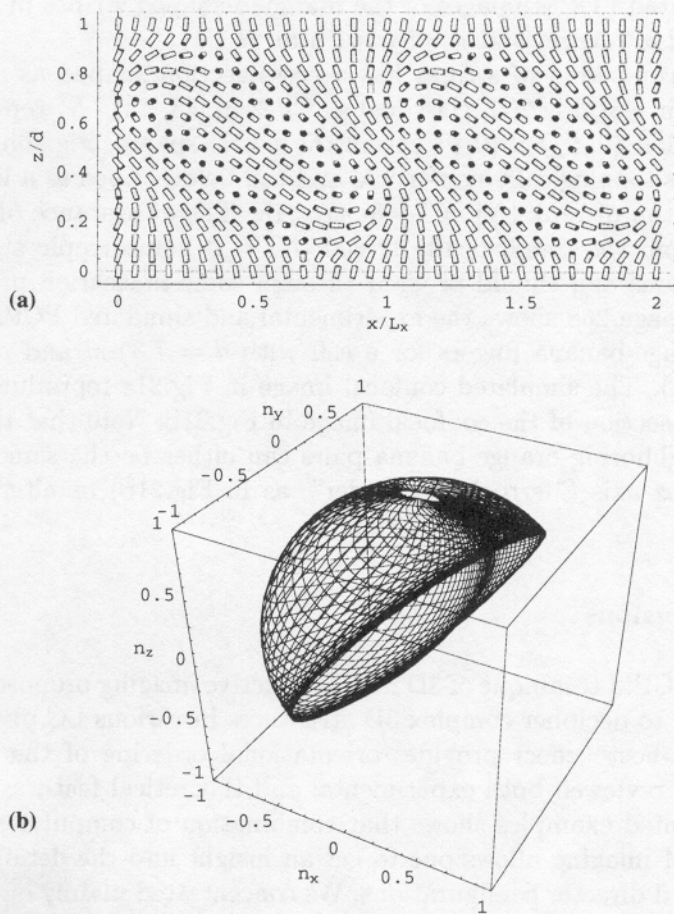In this section we present computer and FCPM studies of cholesteric

Figure 18. Computer simulations of diamond-shaped stripes in a cholesteric cell with homeotropic boundary conditions: (a) director field; (b) S^2 representation. Parameters of simulations: $K_{11} = 6.4$, $K_{22} = 3$, $K_{33} = 10$ and $K_{24} = 0$ (all in pN); $d/p = 1.45$; $W_p d/K_{33} = 15$, zero voltage. The bounding substrates are normal to the axis z.

stripes in homeotropic cells with $C > C_c$. The homeotropic alignment was obtained by lecithin coating of the substrates. We used E7 doped with CB15 to obtain p in the range $3 - 10\,\mu m$. A small amount (0.01% by weight) of Rhodamine 6G perchlorate was added for FCPM studies. The modulated

structures were prealigned along one direction by an in-plane magnetic field.

At least two kinds of stripes with a continuous director field exist when $C = 1 - 1.5$. The first kind of stripes has a diamond-shaped cross-section, Fig.18a, and has been classified as CF-1 in [42, 43, 44]. The mapping of one period $(0, L_x) \times (0, d)$ of the director configuration into the sphere S^2 covers only a part of S^2, Fig.18b. Figure 19 on page 267 shows experimental and simulated FCPM images of the diamond-shaped stripes in a cell with thickness $d = 7.3\,\mu m$, and $p = 5\,\mu m$ (Mau ≈ 1.1).

The second kind of stripes has a cross section shaped as an orange–banana pair [45], Fig.20a, classified as CF-2 in [43, 44]. S^2 representation of one period $(0, L_x) \times (0, d)$ covers the whole sphere, Fig.20b. Thus the structure is topologically non-trivial and can be described as a linear topological soliton of rank $|N| = 1$ [46, 47, 34]. The appearance of the linear solitons from the topologically trivial $|N| = 0$ homeotropic state cannot be continuous and should proceed through some nucleation process. Figure 21 on page 268 shows the experimental and simulated FCPM textures of the orange-banana fingers for a cell with $d = 7.3\,\mu m$ and $p = 5\,\mu m$ (Mau ≈ 1.1). The simulated confocal image in Fig.21c reproduces the vertical cross-section of the confocal image in Fig.21b. Note that the polarity of the neighboring orange-banana pairs can either be the same along the horizontal x-axis ("ferroelectric order", as in Fig.21b) or alternate along the x-axis.

6. Conclusions

The new FCPM technique of 3D non-destructive imaging proposed in [5] is a useful tool to decipher complex 3D structures in various LC phases, where the "guest-host" effect provides orientational ordering of the fluorescent probe. We reviewed both experimental and theoretical features of FCPM. The presented examples shows that combination of computer simulations and FCPM imaging allows one to get an insight into the details of rather complicated director configurations. We concentrated mainly on cholesteric samples as the twisted structures are rather challenging for FCPM imaging because of the non-trivial features of light propagation. The presented examples demonstrate that interpretation of the FCPM textures should take into account the specific parameters of the specimen, such as the Mauguin number Mau $= \frac{p\Delta n}{2\lambda}$. Non-uniform director configurations that result from the balance of bulk chirality, surface anchoring and applied electric field, are mostly accessible for FCPM observations when Mau ~ 1. For large Mau $\gg 1$, some of the twisted configurations (e.g., a configuration in a planar twisted nematic cell) cannot be resolved because of the Mauguin effect. For small Mau < 1, FCPM yields a coarse-grain cholesteric textures
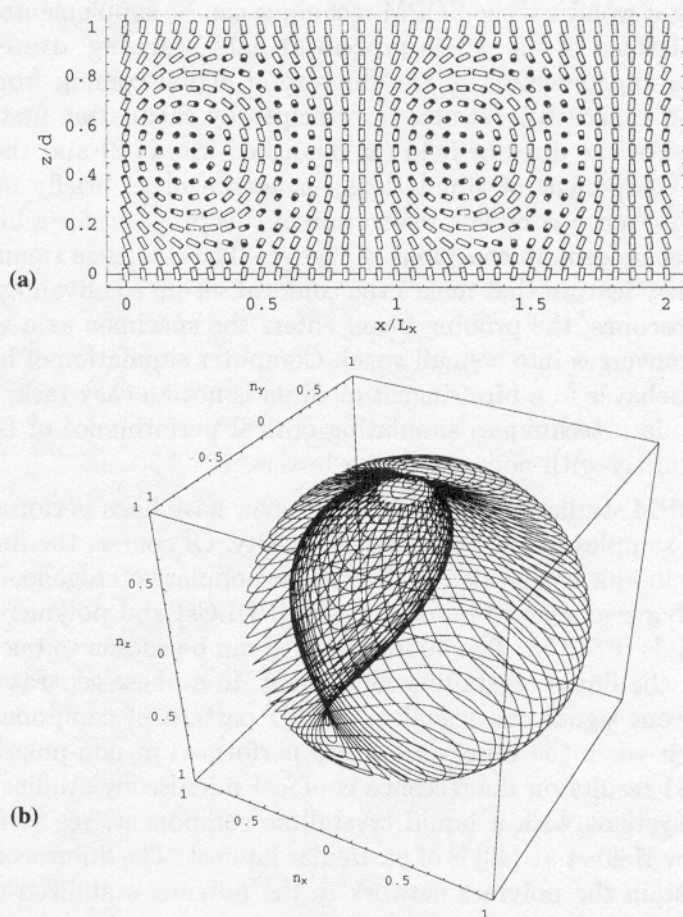
Figure 20. Computer simulations of the stripes with "orange-banana" cross-sections in a cholesteric cell with homeotropic boundary conditions: (a) director field; (b) S^2 representation. Parameters of simulations are the same as in Fig.18.

that image orientation of the helical axis rather than the director field.

Optical anisotropy of LCs makes the resolution of 3D FCPM imaging not as good as one might obtain with the isotropic media. As we repeatedly stressed, the resolution can be improved by using low-birefringence LCs, which are readily available nowadays. Furthermore, even for LCs of high birefringence, say $\Delta n \approx 0.2$, the qualitative director features are still clearly visualized by FCPM, with a good resolution $\sim 1\,\mu m$ for the depth of scanning up to $\sim 10\,\mu m$. The very possibility to take a look at the vertical cross-section of the LC cell overweighs the inconvenience of somewhat worsen resolution.

One might wonder if the FCPM technique can be supplemented by computer simulations of the whole process of light scanning, dye excitation, fluorescence and detection of the fluorescent signal coming from the LC sample. The approach is feasible in principle, by calculating first the computer model of the director field (as described in sect.2) and then adding an optical component of simulations, using the ideas briefly outlined in sect.3.4. However, a complete realization of this program for a birefringent medium is at present an enormous challenge. The challenge stems from the very same key feature that makes the confocal set-up so advantageous over other microscopes: the probing beam enters the specimen as a wide-angle cone that converges into a small voxel. Computer simulation of how such a light cone behaves in a birefringent medium is not an easy task; for example, the modern techniques simulating optical performance of LC display cells deal mostly with non-converging beams.

The FCPM studies presented in this review have been performed on liquid crystal samples with homogeneous density. Of course, the fluorescence confocal technique can be also applied to the popular heterogeneous systems such as polymer-dispersed liquid crystals (PDLCs) and polymer-stabilized liquid crystals (PSLCs). The fluorescent dye can be chosen to tag either the polymer or the liquid crystalline component. In a phase-separated system, the fluorescent signal can visualize the 3D pattern of components distribution, even when the observations are performed in non-polarized light. For detailed results on fluorescence confocal microscopy studies of phase-separated systems with a liquid crystalline component, see Refs. [48-54]. The work by Held et al. [49] is of particular interest. The fluorescent dye was chosen to stain the polymer network in the polymer-stabilized cholesteric liquid crystal. The cholesteric twist imposed on the polymer network was successfully visualized by imaging the polymer network at different depth of scanning in the bulk of the planar cell. As we discussed above, by adding the feature of polarized light observations, the cholesteric twist can be visualized even when the sample is filled with a homogeneous LC material. Very recently, Springer and Higgins [55] studied director configurations in nematic droplets in very thin ($\sim 1\,\mu m$) films of PDLC materials by using a polarization-sensitive multiphoton-excited fluorescence imaging technique that employs fluorescence of the LC material itself.

Note that the feature of polarization-sensitivity is also a useful addition to another high-resolution technique, the scanning near-field optical microscopy (SNOM), which is nowadays widely used in the studies of surfaces and very thin films [56]. As recently demonstrated by Roeder et al. [57], the polarization-sensitive SNOM allows one to detect the spatial variation of director at the surface of oligomer cholesteric LC films. In one of the examples in the cited work, the contrast was caused by changes in the orientation

of the fluorescent dopant molecules that followed the local director. This is the same "guest-host" effect that allows the FCPM technique to pick up the director features in the whole bulk of the sample, as described in this review and in Ref.[5].

Despite some limitations of the FCPM outlined above, the technique literally adds a new ("z") dimension to the study of various systems with liquid crystalline order and we have little doubts that it will be widely used.

7. Acknowledgements
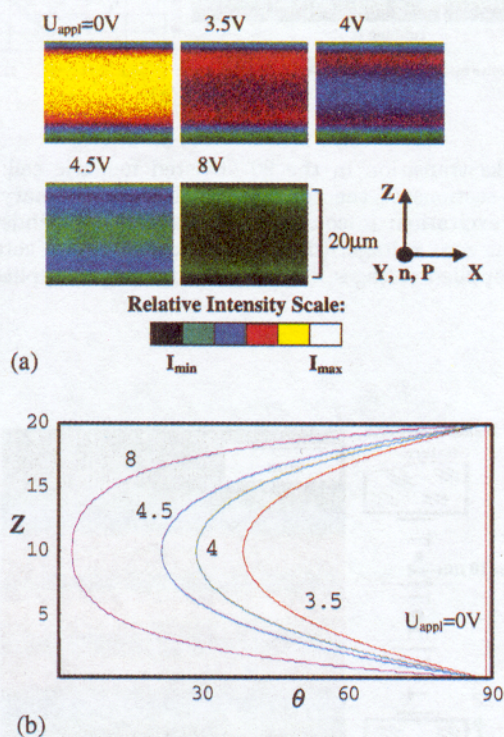
Figure 5. Fredericks transition in the non-twisted nematic cell: (a) FCPM textures of the vertical cross-sections of the cell for different applied voltages; (b) computer simulations of the angle θ between the surface normal and the director.
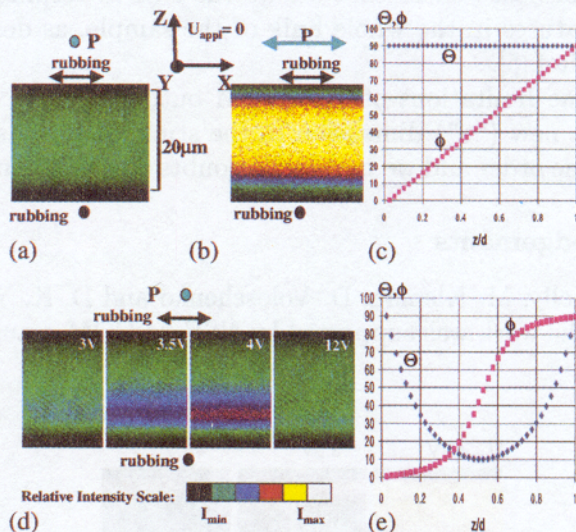
Figure 6. Fredericks transition in the 90^0 twisted nematic cell: (a) FCPM texture of the vertical cross-sections of the cell in zero field for ordinary excitation; (b) the same, extraordinary excitation; (c)computer-simulated z - dependencies of polar θ and azimuthal φ angles at zero voltage; (d) FCPM textures of the vertical cross-section of the cell for different applied voltages; (e) the same functions, applied voltage 4V.
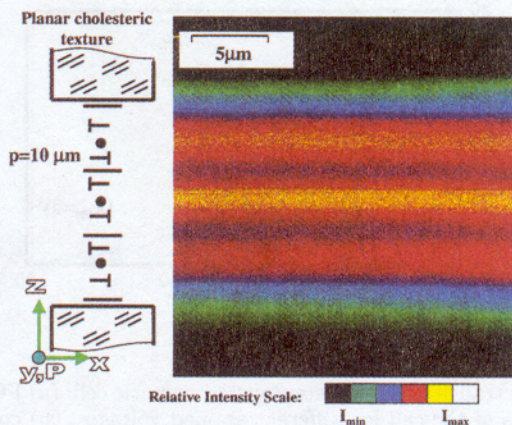

Figure 7. FCPM image of the vertical cross-section of a planar cholesteric cell with a uniform twist. Objective 60×, NA = 1.4.
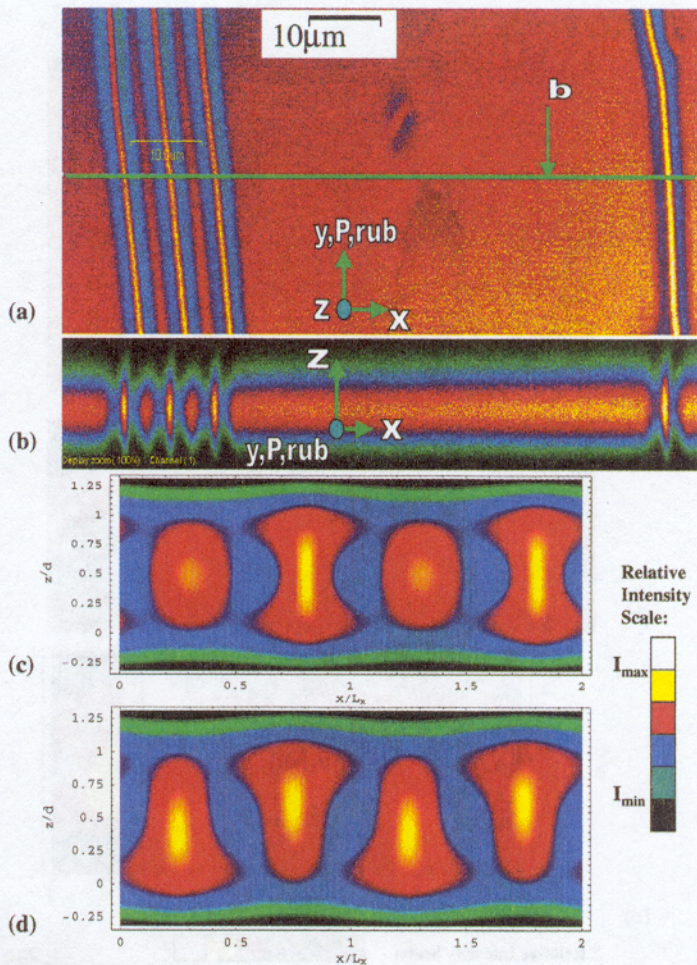
Figure 15. FCPM images of the parallel stripes (I) in a cholesteric cell with a planar anchoring under the *AC* - voltage of $1.6V$: (a) real-experiment FCPM image of the middle (x,y) plane of the cell; (b) real-experiment FCPM texture of the vertical cross-section of the cell; (c) computer simulated FCPM texture of the "O" structure that matches the observed FCPM texture in (b); (d) computer-simulated FCPM texture of the "snake" structure that does not match the observed FCPM texture in (b). The bounding plates are normal to the z-axis and the rub direction is along the y-axis.
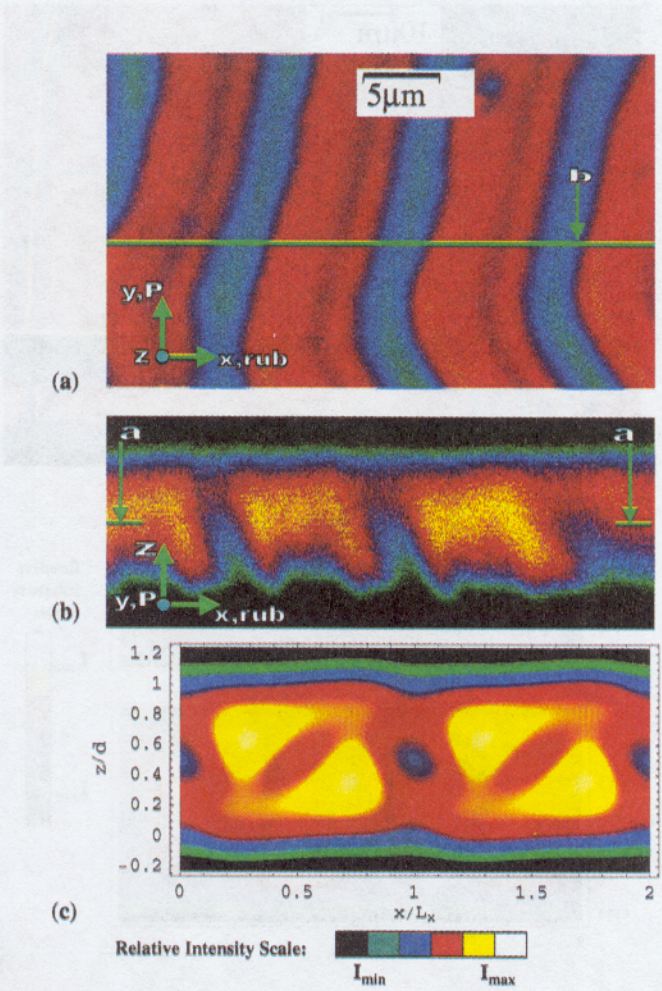
Figure 17. Perpendicular cholesteric stripes (II) in a cholesteric cell with planar anchoring: (a) real-experiment FCPM texture of the middle plane of the sample; (b) real-experiment texture of the vertical cross section of the cell; (c) computer-simulated FCPM image of the director structure shown in Fig.16.
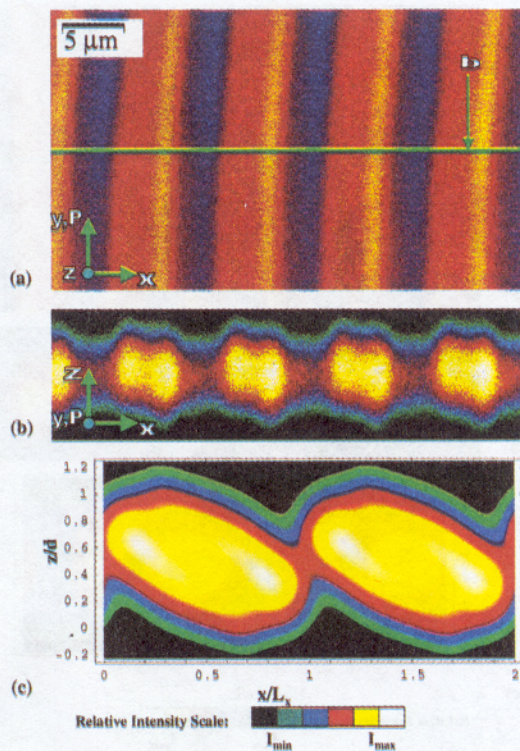
Figure 19. FCPM image of the stripes with the diamond-shaped cross-section in a cholesteric cell with homeotropic boundary conditions: (a) real-experiment FCPM texture of the middle horizontal (x, y) plane of the sample; (b) real-experiment FCPM texture of the vertical cross-section of the cell; (c) computer simulated FCPM image of the director field in Fig.18. Cell thickness $d = 7.3\,\mu m$, pitch $p = 5\,\mu m$.
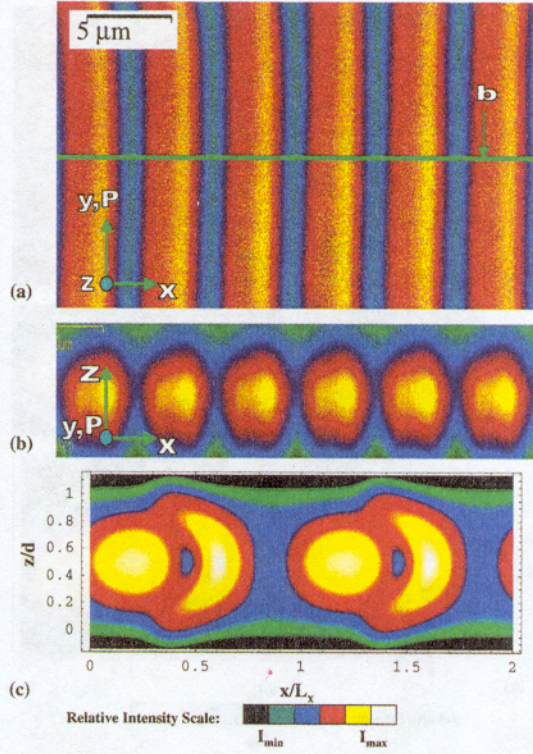
Figure 21.   FCPM images of the stripes with "orange-banana" cross-sections in a cholesteric cell with homeotropic boundary conditions: (a) real-experiment FCPM texture of the middle horizontal (x, y) plane of the sample; (b) real-experiment FCPM texture of the vertical cross-section of the cell; (c) computer simulated FCPM image of the director field in Fig.20. Cell thickness $d = 7.3\,\mu m$, pitch $p = 5\,\mu m$.

References

1. de Gennes, P.G. and Prost, J. (1993) *The Physics of Liquid Crystals*. Clarendon Press, Oxford.
2. Hartshorn, N.H. (1974) *The Microscopy of Liquid Crystals*. Microscope Publications, London.
3. Haudin, J.M. (1986) in *Optical Properties of Polymers*, Meeten, G.H. (ed.) Elsevier, Essex, p. 167.
4. Bellare, J.R., Davis, H.T., Miller, W.G. and Scriven, L.E. (1990) *J. Coll. Interf. Sci.* **136**, 305.
5. Smalyukh, I.I., Shiyanovskii, S.V. and Lavrentovich, O.D. (2001) *Chem. Phys. Lett.*, **336**, 88.
6. C. Bahr and H. Kitzerow, (ed.) (2001) *Chirality in Liquid Crystals*. Springer-Verlag, New York.
7. de Gennes, P.G. (1971) *Mol. Cryst.Liq.Cryst.* **12**, 19.
8. Lubensky, T.C. (1970) *Phys. Rev. A*, **2**, 2497.
9. Kilian, A. and Hess, S. (1990) *Liquid Crystals*, **8**, 465; Sonnet, A., Kilian, A. and Hess, S. (1995) *Phys. Rev. E*, **52**, 718; Hess, S. (2001) this book.
10. Berreman, D.W. and Meiboom, S. (1983) *Phys. Rev. A*, **30**, 1955.
11. Poniewerski, A. and Sluckin, T.J. (1985) *Mol.Phys.*, **55**, 1113.
12. Longa, L. and Trebin, H.-R. (1989) *Phys. Rev. A*, **15**, 2160.
13. Rapini, A. and Papoular, M. (1969) J. Phys. (Paris) Colloq. **30**, C-4.
14. Sugimura, A., Luckhurst, G.R. and Ou-Yang, Z. (1995) *Phys. Rev. E*, **52**, 681.
15. Shiyanovskii, S.V., Glushchenko, A., Reznikov, Yu., Lavrentovich, O.D. and West, J.L.(2000) *Phys. Rev. E*, **62**, R1477.
16. Nobili, M. and Durand, G. (1992) *Phys. Rev. A*, **46**, R6174.
17. Šarlah, A. and Žumer, S. (1999) *Phys. Rev. E*, **60**, 1821.
18. See, e.g., R.H. Webb, *Rep. Prog. Phys.* **59**, 427 (1996); W.T. Mason, (ed.) (1999) *Fluorescent and Luminescent Probes for Biological Activity: a Practical Guide to Technology for Quantitative Real Time Analysis*. Calif.:Academic Press, San Diego; Pawley, J.B. (ed.) (1995) *Handbook of Biological Confocal Microscopy*. Plenum Press, New York.
19. Lavrentovich, O.D. and Yang, D.-K. (1997) *ALCOM Symposium on Reflective Displays, Dec.11-12, 1997, Cuyahoga Falls, Ohio*, vol. IX, p. 11-21.
20. Lavrentovich, O.D., Shiyanovskii, S.V. and Voloschenko, D. (1999) *Proc. SPIE*, **3787**, 149.
21. Voloschenko, D. and Lavrentovich, O.D. (2000) *Opt. Lett.* **25**, 317.
22. Blinov, L.M. and Chigrinov, V.G. (1994) *Electrooptic Effects in Liquid Crystal Materials*. Springer, New York.
23. Janossy, I. (1994) *Phys. Rev. E*, **49**, 2957.
24. Shiyanovskii, S.V. and Terentieva, Ju.G. (1994) *Phys. Rev. E*, **49**, 916.
25. Agranovich, V.M. (1974) Usp. Fiz. Nauk (USSR) **112**, 143; Aver'yanov, E.M. and Osipov, M.A. (1990) *ibid.*, **160**, 89.
26. Davydov, A.S. (1971) *Theory of Molecular Excitons*. Plenum Press, New York; Rashba, E.I. and Sturge, M.D. (1982) *Excitons*. Elsevier, New York.
27. Sugakov, V.I. and Shiyanovskii, S.V. (1980) *Opt. Spektrosk. (USSR)* **48**, 542; Shiyanovskii, S.V. (1981) *Ukrainian Phys. Journ. (Russ. Ed.)* **26**, 137 .
28. Born, M. and Wolf, E. (1970) *Principles of Optics*. Pergamon, Oxford, UK.
29. Gibson, S. and Lanni, F. (1992) *J. Opt. Soc. Am. A*, **9**, 154.
30. Bur, A.J., Roth, S.C. and Thomas, S.C. (2000) *Rev. Sci. Instr.* **71**, 1516.
31. Yeh, P. and Gu, C. (1999) *Optics of Liquid Crystal Displays*. Wiley, New York.
32. Belyakov, V.A. and Sonin, A.S. (1982) *Optika holestericheskih zhidkih kristallov*. Nauka, Moscow.
33. Kleman, M. (1983) *Points, Lines and Walls in Liquid Crystals, Magnetic Systems and Various Ordered Media*. Wiley, Chichester.

34. O.D. Lavrentovich and M. Kleman(2001), Ch.5: Cholesteric Liquid Crystals: Defects and Topology, in: *Chirality in Liquid Crystals*, Bahr, C. and Kitzerow, H. (eds.), Springer-Verlag, New York.

35. Li, Z. and Lavrentovich, O.D. (1994) *Phys. Rev. Lett.,* **73**, 280.

36. Boltenhagen, P., Lavrentovich, O. and Kleman, M. (1991) *J. Phys. II, France* **1**, 1233.

37. Lavrentovich, O.D. and Yang, D.-K. (1998) *Phys. Rev. E,* **57**, R6269.

38. Nastishin, Yu.A., Polak, R.D., Shiyanovskii, S.V., Bodnar, V.H. and Lavrentovich, O.D. (1999) *J. Appl. Phys.* **86**, 4199.

39. Subacius, D., Shiyanovskii, S.V., Bos, Ph. and Lavrentovich, O.D. (1997) *Appl. Phys. Lett.* **71**, 3323.

40. Shiyanovskii, S.V., Subacius, D., Voloschenko, D., Bos, Ph. and Lavrentovich, O.D. (1998) *Proc. SPIE,* **3475**, 56.

41. Lequeux, F. (1988) *J. Phys. France* **49**, 967.

42. Baudry, J., Pirkl, S. and Oswald, P. (1998) *Phys. Rev. E,* **57**, 3038.

43. Oswald, P., Baudry, J. and Pirkl, S. (2000) *Phys. Reports,* **337**, 67.

44. Baudry, J., Pirkl, S. and Oswald, P. (1999) *Phys. Rev. E,* **59**, 5562.

45. Gil, L. and Gilli, J.M. (1999) *Phys. Rev. Lett.,* **59**, 5562.

46. Dubrovin, E.A., Novikov, S.P. and Fomenko, A.E. (1990) *Modern Geometry: Methods and Applications.* Springer, New York.

47. Mineev, V.P. and Volovik, G.E. (1978) *Phys. Rev. B* 18, 3197.

48. White, W.R. and Wiltzius, P. (1995) *Phys. Rev. Lett.,* **75**, 3012.

49. Korlach, J., Schwille, P., Webb, W.W. and Feigenson, G.W. (1999) *Proc. Natl. Acad. Sci. USA* **96**, 8461.

50. Held, G.A., Kosbar, L.L., Dierking, I., Lowe, A.C., Grinstein, G., Lee, V. and Miller, R.D. (1997) *Phys. Rev. Lett.,* **79**, 3443.

51. Nephew, J.B., Nihei, T.C. and Carter, S.A. (1998) *Phys. Rev. Lett.,* **80**, 3276.

52. Amudson, K., van Blaaderen, A. and Wiltzius, P. (1997) *Phys. Rev. E,* **55**, 1646.

53. Blonk, J.C.G., van de Pas, J.C., Visser, A. and Brouwn, L.F. (1998) *Colloids and Surfaces,* **A144**, 287.

54. Tahara, S., Niiyama, S., Kumai, H. and Wakabayashi, T. (1998) *Proc. SPIE,* **3297**, 44.

55. Springer, G.H. and Higgins, D.A. (2000) *J. Am. Chem. Soc.,* **122**, 6801.

56. Paesler, M.A. and Moyer, P.J. (1996) *Near-field Optics.* Wiley, New York.

57. Röder, Th., Paelke, L., Held, N., Vinzelberg, S. and Kitzerow, H.-S. (2000) *Rev. Sci.Inst.,* **71**, 2759.